Earliest human burial in Africa

María Martinón-Torres[1,2]*, Francesco d'Errico[3,4], Elena Santos[5], Ana Álvaro Gallo[1], Noel Amano[6], William Archer[7,8,9], Simon J. Armitage[10,4], Juan Luis Arsuaga[5,11], José María Bermúdez de Castro[1,2], James Blinkhorn[10,6], Alison Crowther[6,12], Katerina Douka[6,13], Stéphan Dubernet[14], Patrick Faulkner[15,6], Pilar Fernández-Colón[1], Nikos Kourampas[16,17], Jorge González García[18], David Larreina[1], François-Xavier Le Bourdonnec[14], George MacLeod[17], Laura Martín-Francés[1], Diyendo Massilani[19], Julio Mercader[20,6], Jennifer M. Miller[6], Emmanuel Ndiema[21,6], Belén Notario[1], Africa Pitarch Martí[3,22], Mary E. Prendergast[23], Alain Queffelec[3], Solange Rigaud[3], Patrick Roberts[6,12], Mohammad Javad Shoaee[6], Ceri Shipton[24,25], Ian Simpson[17], Nicole Boivin[6,12,20,26]* & Michael D. Petraglia[6,12,27]*

[1]CENIEH (Centro Nacional de Investigación sobre la Evolución Humana), Paseo de la Sierra de Atapuerca 3, 09002, Burgos, Spain.

[2]Anthropology Department, University College London, 14 Taviton Street, London WC1H 0BW, UK.

[3]UMR 5199 CNRS De la Préhistoire à l'Actuel: Culture, Environnement, et Anthropologie (PACEA), Université Bordeaux, Allée Geoffroy Saint Hilaire, CS 50023 F - 33615 Pessac CEDEX, Talence, France.

[4]SFF Centre for Early Sapiens Behaviour (SapienCE), University of Bergen, Post Box 7805, 5020, Bergen, Norway.

[5]Centro Mixto UCM-ISCIII de Evolución y Comportamiento Humanos, Instituto de Salud Carlos III, 28029, Madrid, Spain.

[6]Department of Archaeology, Max Planck Institute for the Science of Human History, Kahlaische Strasse, 07745, Jena, Germany.

[7]Department of Archaeology and Anthropology, National Museum, Bloemfontein, South Africa.

[8]Department of Archaeology, University of Cape Town, South Africa.

[9]Department of Human Evolution, Max Planck Institute for Evolutionary Anthropology, Leipzig, Germany.

[10]Department of Geography, Royal Holloway, University of London, Egham, Surrey, TW20 OEX, UK.

[11]Departamento de Paleontología, Facultad de Ciencias Geológicas, Universidad Complutense de Madrid, 28040, Madrid, Spain.

[12]School of Social Science, The University of Queensland, St Lucia QLD 4072, Brisbane, Australia.

[13]Research Laboratory for Archaeology and the History of Art, Dyson Perrins Building, South Parks Road, Oxford, OX1 3QY, UK.

[14]UMR 5060 CNRS-Université Bordeaux Montaigne IRAMAT-CRP2A: Institut de recherche sur les Archéomatériaux – Centre de recherche en physique appliquée à l'archéologie, Maison de l'archéologie, Esplanade des Antilles, 33607 Pessac Cedex, France.

[15]Faculty of Arts and Social Sciences, Department of Archaeology, The University of Sydney, Sydney, NSW, Australia.

[16]Centre for Open Learning, University of Edinburgh, Paterson's Land, Edinburgh, EH8 8AQ, Scotland, UK.

[17]Biological and Environmental Sciences, University of Stirling, Stirling, FK9 4LA, Scotland, UK.

[18]3D Applications Engineer and Heritage Specialist Digital Heritage and Humanities Collections. University of South Florida, 4202 E. Fowler Ave., LIB 122, Tampa, Florida, USA.

[19]Department of Evolutionary Genetics, Max Planck Institute for Evolutionary Anthropology, Leipzig, Germany.

[20]Department of Anthropology and Archaeology, University of Calgary, 2500 University Drive, Calgary, AB, T2N 1N4, Canada.

[21]National Museums of Kenya, Department of Earth Sciences, Nairobi, Kenya.

[22]Seminari d'Estudis i Recerques Prehistòriques (SERP), Facultat de Geografia i Història, Departament d'Història i Arqueologia, Universitat de Barcelona, Montalegre 6, 08001, Barcelona, Spain.

[23]Department of Sociology and Anthropology, Saint Louis University, Avenida del Valle 34, Madrid, Spain.

[24]Institute of Archaeology, University College London, Gordon Square, WC1H 0PY, U.K.

[25]Centre of Excellence for Australian Biodiversity and Heritage, The Australian National University, Canberra, Australia.

[26]Department of Anthropology, National Museum of Natural History, Smithsonian Institution, Washington, D.C., 20560, USA.

[27]Human Origins Program, National Museum of Natural History, Smithsonian Institution, Washington, D.C., 20560, USA.

[*] Corresponding authors

The origin and evolution of mortuary practices are topics of intense interest and debate. Human burials dated to the African Middle Stone Age (MSA) are exceedingly rare, and unknown in East Africa. Here, we describe the partial skeleton of a c. 2.5-3.0 year-old child dating to 78.3 ± 4.1 ka, recovered in the MSA layers of Panga ya Saidi (PYS), an archeological site in the tropical upland coast of Kenya. Recent excavations revealed a pit feature containing a child in a flexed position. Taphonomic, geochemical, granulometric, and micromorphological analyses of the burial pit content and encasing archaeological layers indicate that the pit was deliberatly excavated. Strict articulation or good anatomical association of the skeletal elements and histological evidence of putrefaction support the in-place decomposition of the fresh body. Absent to minimal

displacement of the unstable joints during decomposition points to an interment in a filled space (grave earth) making PYS the oldest human burial in Africa. The morphological assessment of the partial skeleton is consistent with its assignment to *H. sapiens*, although the preservation of some primitive features in the dentition supports increasing evidence for non-gradual accretion of modern traits during the emergence of our species. The burial sheds new light on how MSA populations interacted with the dead.

Increasing scrutiny is being placed on the interplay between biological and cultural factors in the evolution of our lineage and the emergence of our species in Africa[1-2]. Mortuary practices play a key role in this debate as growing evidence supports an ancient origin and possible long-term evolution of these behaviours. Formal burials, defined as the interment of a dead body in an excavated grave, may have been preceded by more elusive practices and only performed by the latest representatives of our genus. Testing this scenario is made difficult, particularly in Africa, by the scarcity of sites with clear and well-dated evidence of dead body treatement.

Panga ya Saidi (PYS) has emerged as one of the key Middle Stone Age (MSA) and Later Stone Age (LSA) sites of Africa given its excellent preservation of environmental proxies which demonstrate its unique long-term position in a coastal tropical forest-grassland ecotone[5,6], as well as its distinctive and continuous sequence of technological innovations and symbolic traits[6,7]. The excavated cave sequence is ~3 metres deep and encompasses 19 layers (Fig. 1). A series of 20 stratigraphically ordered radiocarbon and optically stimulated luminescence (OSL) ages, when included in a Bayesian model, indicate human occupation from ~78 ka to 500 years ago[6], including in each of the last five marine isotope stages.

The 2013 excavations at PYS revealed a partial pit feature in profile, markedly contrasting in texture and colour in comparison to the surrounding matrix (Fig. 1, Supplementary Information A). An OSL tube (OSL4) and a micromorphology sample (PYS 13_1) were placed in the feature in 2013. Upon removal, the micromorphology sample revealed the presence of heavily degraded bones inside the section. Excavations were expanded in 2017 to expose the top of the feature, which was positioned at the bottom of MSA Layer 18. The plan view of the pit was subcircular, measuring 36.7 cm (north-south) x 39.8 cm (west-east) x 12.5 cm (depth) (Fig. 1b, Supplementary Information A). Limited hand excavation at the top of the pit indicated that the feature contained a concentration of fragile and degraded bones in association with MSA lithic artefacts (Extended Data Fig. 1, Supplementary Information B), embedded in a matrix different from the surrounding sediments of Layer 19 (Supplementary Information A). The excavation surface indicated the presence of decomposed bones, in what was later shown to be the base of a skull and an articulated spine of a child (Fig. 1b).

Several small fragments of unidentified bone were recovered during the 2017 excavation but due to their poor state of preservation, it was decided to plaster the whole feature and transport it for careful laboratory excavation. The plastered remains were first taken to the National Museums of Kenya (NMK) in Nairobi, and then to the Conservation and Restoration laboratories at CENIEH in Burgos, Spain. The low density and extreme fragility of the bones necessitated a combination of mechanical and digital cleaning (Supplementary Information A).

Careful examination revealed the articulated partial skeleton of an immature human (Fig. 2). Sample OSL4, taken directly from the feature in 2013, was processed at Royal Holloway, London, resulting in a stratigraphically coherent age of ~76.0 ± 7.4 ka Incorporation of this OSL age into the Bayesian model yielded an estimated age of 78.3

± 4.1 ka for the pit (Extended Data Fig. 2, Supplementary Information C). Hand excavation of the sediment block encasing the skeletal elements revealed the presence of lithics and fauna (Supplementary Information B, Extended Data Fig. 1) consistent with the surrounding layers. These layers (18 and 19) produced a large assemblage of artefacts (n=2194) that have been shown to be both distinct from the LSA layers above (16-1) (Shipton et al. 2018) and consistent with other MSA assemblages in East Africa (Blinkhorn and Grove 2018; Grove and Blinkorn 2020), thereby providing additional and robust proof that the pit was associated with MSA occupations. Screening of the sediment and skeletal elements for ancient DNA proved inconclusive (Supplementary Information D).

As explained below, the field and laboratory evidence strongly indicates that this is a primary and intentional burial, and that the child's body was deliberately placed in an excavated pit that was posteriorly and rapidly backfilled with sediment.

Primary and intentional deposit

The skeletal remains consist of a considerable part of the basicranium, a fragment of the left hemi-mandible with a complete ramus, five teeth (right M_1, right M^1, left dm^2 and the *in situ* and un-erupted left M_1 and left M^1), the cervical and thoracic spine with associated ribs, the right clavicle, and the left humerus (Fig. 2). Beyond these better-preserved bones, there were several fragments corresponding to the cranial, facial, pectoral, pelvic and limb areas, although anatomical identification is difficult due to the severe diagenesis (bioerosion, recrystallisation) of the skeleton (Extended Data Figs. 3-4, Extended Data Table 1, Supplementary Information E). Fragments of the left radius and ulna (in anatomical connection through a lump of sediment), and a deformed fragment of the left parietal, were also recovered from the burial fill, although detached from the main block (Supplementary Information A). Several unidentifiable small, white and flat bone fragments recovered in the field, prior to plastering the feature, probably correspond to the crushed and severely distorted upper part of the cranial vault. The advanced diagenesis of the bones prevented the preservation and/or physical recovery of the remaining skeletal elements. Photographs taken after micromorphology sampling in 2013 show the proximal portion of the right femora inside the section (see Supplementary Information A Fig. 2) and photographs of the plan view in 2017 show the proximal end of the left femur (Fig. 1 b) . Based on dental development we estimate that the child, which we named 'Mtoto' ('child' in Swahili), died at the age of 2.5-3.0 years (Supplementary Information F).

According to Duday (2006), the identification of a primary burial (the fresh body was placed in a location where the entire process of decomposistion took place) is based on four criteria: i) the macroscopic anatomical integrity of the body, specially of unstable articulations; ii) the minimal displacement of the bones that can be explained within the course of decompostition; iii) abundance of terrestrial gastropods that feed on earthworms in close proximity to the corpse and iv) geochemical and histological analyses in favour of an ins situ-decomposition and putrefaction. All these criteria are met with the PYS finding.

The majority of the bones appear in either strict articulation or in good anatomical association and minor displacements can be explained as a consequence of decomposition and subsequent formation of secondary spaces. The combination of the photographic, microtomographic and surface scanner data, together with the total station coordinates of the feature, confirm that the body was deposited in a flexed right lateral decubitus position with the thighs flexed towards the torso at an angle less than 90º (Fig. 3, Extended Data Fig. 5). The vertebral column forms an arc stretching from the cervical to the distal thoracic area, and this, together with the relative position of the lower limbs, denotes a tightly flexed position of the body. The body is not lying flat, but the spine it is at an angle of approximately 12º above the horizontal axis. The thorax is laterally compressed (Fig.3, Extended Data Fig. 5). The ribs on the right side are flattened and those on the left side are at a higher angulation. There is a gap between the anterior ends of the right and the left ribs from the same vertebral level, consistent with the interpretation that the child was lying on its right side. Although the mechanical pressure of the sediment flattened the thorax, the rib cage did not collapse, preserving the original spatial relationship and curvature of the ribs, pointing to decomposition in a filled space (Supplementary Information A). Indeed, the preservation of most of the thorax articulations and its volume indicates that the destruction of the soft tissues and viscera did not produce a large, temporary empty space. This phenomenon tends to occur in contexts characterised by particularly fluid sediments that infiltrate by percolation and it is indirect but solid evidence of a deposit made in bare earth[10]. The particle size analysis confirms that the sediment inside the burial presents a higher proportion of both silt and sand and a lower proportion of clay in comparison to Layers 17-19 (except for two samples from top of Layer 18; Fig. 4 and Supplementary Information G). This would favour a progressive infilling of the internal space as the cadaver decomposed and reinforces the hypothesis of an in-situ decomposistion of the cadaver.

The right clavicle displays an oblique orientation, with a descent of the sternal extremity of almost 90º (Supplementary Information A). Similarly, the first and second right ribs are also distally displaced, and rotated medially about 90º, but they preserve the intercostal space, arguing in favour of a minimal displacement of the sternal articulation of the pectoral girdle. The depression of the clavicle and the adoption of an oblique orientation are typical of tightly shrouded burial[11]. This is consistent with the upper part of the body being wrapped in a perishable cloth/material, or alternatively, the body being densely packed within its pit structure. In either case, such a deliberate treatment of the body would explain the exceptional in-place preservation of the scapula and humerus of the over-hanging arm, and the intact articulation of the vertebral column and ribs, which would otherwise likely collapse as the decomposition advances [10].

Rotation of the head is common in burials, as a result of the gravity force and the weight of the cranium when the decay of the cranio-vertebral attachments places it in an unstable position (Extended Data Fig. 5). For Mtoto, the cranium and first three cervical vertebrae are disarticulated as a unit and partially dislocated from the column. The movement of the head points to the existence of some empty space around it and it contrasts with the progressive infilling and minimal displacmenet of the rest of the body. In a fresh cadaver, this type of head dislocation involving the cervical vertebrae couldn indicate collapse due to the decay of a perishable support placed beneath the head[12,13]. Mtoto's head dislocation, together with the depression of the clavicle and the first two ribs, would be compatible with the upper part of the body being wrapped and the head supported with a perishable material. The differential preservation of the upper versus the lower part of the body could be additional evidence for this protective treatment. These evidence would be supportive of a more elaborated involvement of the community in the funerary rite versus the structured abandonment (Pettitt, 2010) or the happenstance burial (Deffleur, 1993).

Despite extreme bone fragility, the anatomical integrity and strict articulation of some of the so-called unstable or labile articulations such as those between the vertebrae, between the vertebrae and the ribs, and between the left scapulothoracic articulation and the left temporo-mandibular joint indicate this is a primary and undisturbed deposit[10,11] and that the child was covered with sediment rapidly after its placement. Additionally, taphonomical, histological and geochemical analyses support the in-situ decomposition and putrefaction of 'Mtoto'. The anatomical alignment and advanced diagenesis of Mtoto contrasts with the highly fragmented status and more variable diagenetic conditions of non-human faunal remains recovered from Layers 17-19 (Extended Data Table 2, Supplementary Information H).Taken together, all available evidence argues in favour of rapid burial after death of the individual, protecting the skeleton from intense post-depositional breakage as experienced by the faunal remains in the surrounding layers.

Optical microscopy of bone fragments (probably upper limb) demonstrates that human and non-human bone followed different taphonomic trajectories. Human bone underwent predominantly non-Wedl bioerosion (attributed to bacteria[17,18]) and enlargement of osteocyte lacunae and canaliculi (probably due to fungal, or fungal+bacterial action) (Extended Data Figs. 3-4). Although variable across the sample, bioerosion of the larger human bone fragments was arrested (General Histology Index: 2-3). Pervasive recrystallisation of the bone hydroxyapatite into a Ca-enriched, amorphous or cryptocrystalline calcium phosphate - more advanced in endosteal regions – may be associated with 0.1-1μm-scale bacterial microtunnelling[19]. Fe and Mn oxide deposition - probably bacterially mediated - in bone (and adhering sediment) likely resulted from episodes of waterlogging. The most parsimonious interpretation of human bone diagenesis is that the child's body decomposed as a buried fleshed cadaver, in an episodically waterlogged burial environment (Supplementary Information E). Additionally, the skull of 'Mtoto' presents several star-shaped marks and bore holes indicative of insect and gastropod's activity, compatible with with in-situ decomposition.

Higher concentrations of MnO and CaO in the pit fill are consistent with *in situ* decomposition of the body[15,16]. Micromorphological and histological evidence suggests that, while both Ca, Mn (and Fe) mobilisation were diachronous, calcite and Mn oxide deposition in and around the bone may have been mediated to a significant extent by putrefactive bacteria (Supplementary Information E and Extended Data Figs. 3-4, Extended Data Table 1).

The sediment matrix is devoid of microcharcoal, ash or other (putative) microscopic human inputs. Five land snail shell fragments (*Achatina* sp.) were found in close association with the skeleton, around the occipital area. Although one of the shell fragments bear lines incised by a point, not seen in fragements from the encasing layers (Extended Data Fig. 6, Supplementary Information I), fragments of this genus are also abundant in penecontemporaneous Layer 18 and bear traces of heating and consumption. Thus, the evidence is not sufficient to suggest deliberate placement of shell fragments in the pit. Nevertheless, the *Achatina* shells from the pit are significantly larger in comparison to those from penecontemporaneous Layer 18, indicating that they did not experience intensive breakage from processes such as trampling (Extended Data Fig. 6, Supplementary Information I). Analysis of reddish agglomerates spotted during the excavation of the child's remains showed that they were not anthropogenic in origin and cannot therefore be interpreted as evidence that the child's body or the wrapping that protected it was covered in ochre (Supplementary Information G).

Burial versus funerary caching

Adittional to the placement of the body, the recognition of a burial requires the identification of purposedly excavated burial pit and the posterior intentional covering of the corpse (Pettitt, 2010). The distinction of a new stratum is key to discern a burial from the accommodation of a body in a natural place such as cave fissures or hollows, also known as funerary caching (Gargett, 1999). The excavation of Trench 4 exposed a distinct feature, a well demarcated pit with different colour and density matrix with no comparable counterpart in the remainder of the sequence Supplementary Information A Fig. 1 and 3) which can only have resulted from intestinal digging into layer 19. The sedimentological analyses provides evidence of a clear burial cutting. The burial fill is a ferruginous mix of silt and sand, compositionally similar to the top of Layer 18 and the base of Layer 17, and different from Layer 19 in which the pit appears to have been excavated (Fig. 4, Supplementary Information G). The fine –grained texture of the intraskeletal matrix may be representative of the original composition of the burying sediment, or it may have resulted from infiltration of the sediment between the bones as the cadaver skeletonised. (Supplementary Information E and Extended Data Figs. 3-4, Extended Data Table 1) and compatible with the evidence of a progressive infilling in a deposit made in bare earth The lack of diagnostic flood features of mass flow deposits in the burying sediment (Supplementary Information E) makes unlikely that possibility of the sediment being washed into the pit during a flood event shortly after the deposition of the corpse. Based on the bone microscopical study, the most parsimonious explanation is to interpret that Mtoto's body was deliberately covered using as backfill sediment scooped from the colluvial deposits that made up the Layer 18 cave floor.

In sum, the interpretation for an intentional burial[20,21] of Mtoto is based on: a) the identification of a clear pit feature digged into layer 19, b) the geochemical and granulometric evidence discriminating the burial fill from the surrounding layers and suggesting that sediment gradually filled empty spaces created by the body putrefaction and insect activity, c) the overall completeness and anatomical integrity of the skeleton and the alignment of the body in a tightly flexed position in the pit consistent with a rapid covering after the body's deposition. The taphonomic reconstruction, the sedimentary evidence, and the anatomical positioning are consistent with the burial of a 'fresh' body and its subsequent decomposition in the pit.

Taxonomic assessment

To investigate Mtoto's taxonomic affiliation, the PYS teeth were compared against a large sample of *H. neanderthalensis* and recent and fossil *H. sapiens*. The expression of several crenulations and mesial accessory tubercles make the PYS dm^2 more primitive than recent counterparts (Fig. 5, Extended Data Fig. 7, Supplementary Information F). The morphology of the PYS M^1 samples fall within the range of variation of *H. sapiens*, though it resembles the morphologically more complex Aterian individuals in its pronounced Carabelli expression, the non-reduction and even in the exceptionally large and subdivided hypocones[22]. In both the dm^2 and the M^1, the occlusal polygon is more rhomboidal than in fossil and recent *H. sapiens*, but not as skewed as in Neanderthals (Supplementary Information F). The size cusp sequence of the M^1 falls between recent and Upper Palaeolithic *H. sapiens* on the one hand, and Neanderthals and Qafzeh on the other. Although the morphology of both of the PYS M_1 samples are compatible with that of *H. sapiens*, the profuse crenulation of their enamel makes this morphology more complex than that of recent *H. sapiens* and some fossil *H. sapiens* specimens such as those from Die Kelders in South Africa, Dolni Vestonice and Pavlov in Europe, Qafzeh and Misliya in the Levant, and Daoxian and Tubo in China[23,24]. The size cusp sequences in the M_1s are intermediate between that found in early *H. sapiens* specimens (Qafzeh H4, Les Rois, Abri Pataud, Dolni

Vestonice DV14) and in Neanderthals and recent *H. sapiens*[25]. The geometric-morphometric shape analysis of the occlusal outline of the EDJ reveals that all teeth cluster with *H. sapiens* except for the M_1 that is closer to the Neanderthal distribution in the inward location of the metconid tip and the more rounded lingual profile (Fig. 5).

The dimensions of Mtoto's teeth fall within the range of variation of recent *H. sapiens* and are smaller than those of Neanderthals and some fossil *H. sapiens* such as Qafzeh and Mesolithic teeth. The enamel of both deciduous and permanent molars of PYS is thick, a primitive condition shared with *H. sapiens* and the majority of speciments in the hominin fossil record except for Neanderthals (Supplementary Information F).

Overall, Mtoto's dentition is consistent with an assignment to *H. sapiens,* although it preserves some primitive features indicating that the child was less morphologically derived than other broadly contemporaneous populations (Supplementary Information F). The mandibular ramus shows a symmetric mandibular notch, where the condylar and coronoid processes are levelled. This, together with the very arched temporal squama, also align Mtoto with *H. sapiens*.

Implications of the PYS burial for human evolution

Despite Africa's alleged centrality for the emergence of 'modern human behaviour' in the Pleistocene[3,26], evidence for morturay practices in the continent is scarce and often ambigous. Intentional defleshing has been inferred from the orientation and location of cut marks on the 600 kyr old Bodo skull, attributed to *Homo heidelbergensis/H. rhodesiensis.* Defleshing and curation, supported by the presence of both diagnostically located cutmarks and polishing are recorded on the skull of the juvenile individual from

Herto. Furthermore, evidence pointing to *funerary caching* - - the deposition of corps in an existing natural feature– has been proposed for the Atapuerca-Sima de los Huesos hominins and *H. naledi* Until now, one of the earliest possible burials in Africa was the infant hominin (BC3) found in 1941 at Border Cave, South Africa, thought to date to ~74 ± 4 ka[27] and apparently associated with a perforated and ochred *Conus* shell. Although recent reappraisal of the evidence confirms the presence of a pit, documentation on this burial is limited. No information is available on the degree of articulation and the position of the remains[28,29] within the pit and its age is inferred from a stratigraphic correlation with a section, dated by ESR, located more than 10 m far from the pit. The chronological and stratigraphic data for the BC3 specimen is coherent overall with an age not younger than 58 ka[27], and possibly as old as 74 ka, but a more constrained chronology for the skeleton is not available.

In contrast to the situation at Border Cave, the contextual, chronological and taphonomic information at PYS are all supportive of a primary burial and meet the criteria for simple, early inhumations of hominins in the Late Pleistocene[21]. On the basis of multiple, and stratigraphically coherent, OSL dates, PYS represents the earliest unequivocal evidence of an intentional burial in Africa at 78.3 ± 4.1 ka, clearly demonstrating that complex treatment of the dead was practiced by *H. sapiens* by late MIS 5. Moreover, the PYS burial reveals a clear and direct association between *H. sapiens* and MSA technology, providing further confirmation of the link between this technology and our early members of our species (Righter et al. 2017).

The PYS child in Kenya, in combination with the infant burial from Border Cave and the funerary caching or interment of a juvenile at Taramsa in Egypt ~69 ka[30], suggests that *H. sapiens* were intentionally preserving the corps of young members of their groups at this time. Prior to ~74.6 ka, however, there are no unambiguous burials of *H. sapiens* in Africa, despite the fact that earlier MSA populations demonstrate sophisticated forms of symbolic expression[31–34]. The absence of burials from the onset of the MSA by 305 ka[35], and the rare occurrence of burials after 74 ka, may be a consequence of cultural choice, such as the disposal of bodies away from residential sites and in ways that are not consistent with their preservation. It may also indicate a shift, sometime between 150 ka and 80 ka, from defleshing and curation, recorded at Herto, to funerary caching and burials, observed at more recent sites from East Africa.

Interestingly, this provides a point of contrast with Neanderthals and early *H. sapiens* outside of Africa, who buried their dead in residential sites by ~120 ka[36], about 45,000 years before PYS, suggesting that intentional burial may have emerged in multiple hominin lineages. Infant and child burials are ubiquitous in Neanderthal and early *H. sapiens* sites in the Levant and Europe, comprising 55-35% of all known interments after 120 ka[36]. Burial in residential localities, such as at PYS, has been suggested to reflect mourning behaviour and the intention to keep the dead nearby[36]. Despite being the cradle of *H. sapiens*[37], Africa demonstrates a scarcity of mortuary practices over most of the MSA that provides little current support for modern-like conceptions of the afterlife and/or treatment of the dead. Nonetheless, cross-cultural evidence in *H. sapiens* clearly emphasises that the absence of a behaviour does not necessarily imply that capacity for such behaviour was lacking. Evidence for advanced planning and symbolism from ~320 ka and particularly after 100 ka at East African sites[38] suggests that modern cultural traits gradually permeated through those societies. Limited evidence for mortuary behaviours in Africa may be due to practices leaving elusive archaeological traces, taphonomy, or limited investigation. The highly fragile and taphonomically-altered nature of the PYS skeletal remains highlight the problematic conservation issues at even a well-preserved site. However, in the light of the available evidence, the possibility of a non-African origin for the burial culture cannot be discarded.

Beyond providing evidence for the earliest clear *H. sapiens* burial in Africa, the ~74.6 ka skeletal remains are also of interest for the insight they provide into the evolution of our species. While the mandibular and dental assessment of Mtoto are consistent with its assignment to *H. sapiens*, the preservation of some primitive dental features in comparison to other penecontemporaneous populations, suggests that our species may have evolved in subidivided and regionally distinct populations and in a variety of paleocological settings (Supplementary Information J). Our study suggests that the biological and socio-cultural evolution of *H. sapiens* was as a complex, likely nonlinear and regionally diverse process.

References

1. Scerri, E. M. L. *et al.* Did our species evolve in subdivided populations across Africa, and why does it matter? *Trends Ecol. Evol.* **33**, 582–594 (2018).
2. Mounier, A. & Lahr, M. M. Deciphering African late Middle Pleistocene hominin diversity and the origin of our species. *Nat. Commun.* **10**, 3406 (2019).
3. McBrearty, S. & Brooks, A. S. The revolution that wasn't: a new interpretation of the origin of modern human behavior. *J. Hum. Evol.* **39**, 453–563 (2000).
4. *Homo symbolicus: The Dawn of Language, Imagination and Spirituality*. (John Benjamins, 2011).

5. Roberts, P. *et al.* Late Pleistocene to Holocene human palaeoecology in the tropical environments of coastal eastern Africa. *Palaeogeogr. Palaeoclimatol. Palaeoecol.* **537**, 109438 (2020).
6. Shipton, C. *et al.* 78,000-year-old record of Middle and Later Stone Age innovation in an East African tropical forest. *Nat. Commun.* **9**, 1832 (2018).
7. d'Errico, F. *et al.* Trajectories of cultural innovation from the Middle to Later Stone Age in eastern Africa: personal ornaments, bone artifacts, and ocher from Panga Ya Saidi, Kenya. *J. Hum. Evol.* **141**, 102737 (2020).
8. Prendergast, M. E. *et al.* Reconstructing Asian faunal introductions to eastern Africa from multi-proxy biomolecular and archaeological datasets. *PLoS ONE* **12**, e0182565 (2017).
9. Skoglund, P. *et al.* Reconstructing prehistoric African population structure. *Cell* **171**, 59-71.e21 (2017).
10. Duday, A. L'archéothanatologie ou l'archaéologie de la mort. in *Social Archaeology of Funerary Remains* (eds. Gowland, R. L. & Knüsel, C. J.) 30–56 (Oxbow Books, 2009).
11. Knüsel, C. J. Crouching in fear: terms of engagement for funerary remains. *J. Soc. Archaeol.* **14**, 26–58 (2014).
12. Kapandii, I. A. *Physiologie Articulaire: Schémas Comment Mécanique Humaine*. vol. 3: Tronc et Rachis (Maloine, 1972).
13. Blaizot, F. Les espaces funéraires de l'habitat groupé des Ruelles à Serris du VIIe au XIe siècles Seine et Marne, Iˆle-de-France): taphonomie du squelette, modes d'inhumation, organisation et dynamique. (Université de Bordeaux, 2011).

14. Backwell, L. R., Parkinson, A. H., Roberts, E. M., d'Errico, F. & Huchet, J. B. Criteria for identifying bone modification by termites in the fossil record. *Palaeogeogr. Palaeoclimatol. Palaeoecol.* **337–338**, 72–87 (2012).
15. Ghiorse, W. C. The biology of manganese transforming microorganisms in soil. in *Manganese in Soils and Plants* (eds. Graham, R. D., Hannam, R. J. & Uren, N. C.) 75–85 (Springer Netherlands, 1988).
16. Thompson, I. A., Huber, D. M., Guest, C. A. & Schulze, D. G. Fungal manganese oxidation in a reduced soil. *Environ. Microbiol.* **7**, 1480–1487 (2005).
17. Jans, M. M. E. Microbial bioerosion of bone: a review. in *Current Developments in Bioerosion* (eds. Wisshak, M. & Tapanila, L.) 397–404 (Springer, 2008).
18. Booth, T. The rot sets in: low-powered microscopic investigation of taphonomic changes to bone microstructure and its application to funerary contexts. in *Human Remains: Another Dimension* (eds. Thompson, T. & Errickson, D.) 7–28 (Elsevier, 2017).
19. Turner-Walker, G., Nielsen-Marsh, C. M., Syversen, U., Kars, H. & Collins, M. J. Sub-micron spongiform porosity is the major ultra-structural alteration occurring in archaeological bone. *Int. J. Osteoarchaeol.* **12**, 407–414 (2002).
20. Defleur, A. *Les Sépultures Moustériennes*. (Editions de CNRS, 1993).
21. Pettitt, P. *The Palaeolithic Origins of Human Burial*. (Routledge, 2010).
22. Bailey, S. E. & Hublin, J.-J. Did Neanderthals make the Châtelperronian assemblage from La Grotte du Renne (Arcy-sur-Cure, France)? in *Neanderthals Revisited: New Approaches and Perspectives* (eds. Hublin, J.-J., Havarti, K. & Harrison, T.) 191–209 (Springer, 2006).
23. Grine, F. E. Middle Stone Age human fossils from Die Kelders Cave 1, Western Cape Province, South Africa. *J. Hum. Evol.* **38**, 129–145 (2000).

24. Liu, W. *et al.* The earliest unequivocally modern humans in southern China. *Nature* **526**, 696–699 (2015).

25. Martín-Albaladejo, M., Martinón-Torres, M., García-González, R., Arsuaga, J. L. & Bermúdez de Castro, J. M. Morphometric analysis of Atapuerca-Sima de los Huesos lower first molars. *Quat. Int.* **433**, 156–162 (2017).

26. Henshilwood, C. & Marean, C. W. The origin of modern human behavior: critique of the models and their test implications. *Curr. Anthropol.* **44**, 627–651 (2003).

27. d'Errico, F. & Backwell, L. Earliest evidence of personal ornaments associated with burial: the conus shells from Border Cave. *J. Hum. Evol.* **93**, 91–108 (2016).

28. Cooke, H. B. S., Malan, B. D. & Wells, L. H. Fossil man in the Lebombo Mountains, South Africa: the 'Border Cave,' Ingwavuma District, Zululand. *Man* **45**, 6–13 (1945).

29. Beaumont, P. B., de Villiers, H. & Vogel, J. C. Modern man in Sub-Saharan Africa prior to 49000 years BP: a review and evaluation with particular reference to Border Cave. *S. Afr. J. Sci.* 409–419 (1978).

30. Vermeersch, P. M. *et al.* A Middle Palaeolithic burial of a modern human at Taramsa Hill, Egypt. *Antiquity* **72**, 475–484 (1998).

31. d'Errico, F. *et al.* Additional evidence on the use of personal ornaments in the Middle Paleolithic of North Africa. *Proc. Natl. Acad. Sci.* **106**, 16051–16056 (2009).

32. Henshilwood, C., d'Errico, F. & Watts, I. Engraved ochres from the Middle Stone Age levels at Blombos Cave, South Africa. *J. Hum. Evol.* **57**, 27–47 (2009).

33. Henshilwood, C. S. *et al.* An abstract drawing from the 73,000-year-old levels at Blombos Cave, South Africa. *Nature* **562**, 115–118 (2018).
34. Steele, T. E., Alvarez-Fernandez, E. & Hallet-Desguez, E. Personal ornaments in early prehistory: a review of shells as personal ornamentation during the African Middle Stone Age. *Paleoanthropol.* **24**, 24–51 (2019).
35. Richter, D. *et al.* The age of the hominin fossils from Jebel Irhoud, Morocco, and the origins of the Middle Stone Age. *Nature* **546**, 293–296 (2017).
36. Stiner, M. C. Love and death in the Stone Age: what constitutes first evidence of mortuary treatment of the human body? *Biol. Theory* **12**, 248–261 (2017).
37. Scerri, E. M. L., Chikhi, L. & Thomas, M. G. Beyond multiregional and simple Out-of-Africa models of human evolution. *Nat. Ecol. Evol.* **3**, 1370–1372 (2019).
38. Brooks, A. S. *et al.* Long-distance stone transport and pigment use in the earliest Middle Stone Age. *Science* **360**, 90–94 (2018).
39. Stringer, C. The origin and evolution of Homo sapiens. *Phil. Trans. R. Soc. B* **371**, 20150237 (2016).
40. Tryon, C. A. The Middle/Later Stone Age transition and cultural dynamics of Late Pleistocene East Africa. *Evol. Anthropol.* **28**, 267–282 (2019).

Online content

Any methods, additional references, Nature Research reporting summaries, source data, extended data, supplementary information, acknowledgements, peer review information; details of author con- tributions and competing interests; and statements of data and code availability are available at https:

Methods

Dating

Optically stimulated luminescence dating. A suite of seven single-grain optically stimulated luminescence (OSL) ages for PYS were published[6], including a detailed description of the luminescence measurement and data analysis techniques used (their Supplemental Note 3). In the present study, we report an additional OSL age, produced using the method previously described[6] for a sample from the burial infill (sample PYS13-OSL4). Data used to calculate the age for OSL4 are presented in bold in Supplementary Information C Tables 1-3, alongside data from the main publication[6] for comparison. Since all quantities reported here were measured using the same instruments and methods as those reported previously[6], it is reasonable to treat them as internally consistent and therefore comparable. Data for OSL4 are consistent with those for previously reported PYS samples, particularly those for OSL3 and OSL5, which yield contemporaneous ages. Particularly noteworthy is the similarity between the ages for OSL4 (burial infill) and OSL3 and OSL5. If the burial pit had been dug into much older sediments, and then infilled using those sediments, some grains would probably have had their luminescence signal reset during the process. This might be expected to yield a younger age for the burial infill than the surrounding sediments, which is not the case. Similarly, the overdispersion for OSL4 is consistent with that for OSL5, where no evidence for post-depositional disturbance has been found. The similarity in age and overdispersion between samples OSL3-5 does not unequivocally demonstrate that the burial infill is contemporaneous with Layers 17 and 18, since if the pit was backfilled with spoil this might have occurred under subdued light conditions leading to poor luminescence signal resetting. Also, given the ~7% uncertainties on individual ages, archaeologically important differences in age could go unnoticed. Nonetheless, the absence of a discrepancy between the ages and overdispersion of the burial infill and surrounding sediments suggests that the burial is contemporaneous with Layers 17/18, at least at the temporal resolution achievable using luminescence techniques.

Bayesian Modelling and age of the PYS burial. Bayesian modelling enables the relative stratigraphic information recorded during excavation to be formally incorporated into posterior age estimates deriving from chronometric data expressed as probability distributions (in this case calibrated radiocarbon and OSL probability distributions) and 'prior' information, i.e. observations on the data we collect. In archaeology, this is often the stratigraphic and other relative information. Hence 'posterior' data, is a probability function that reflects the level of confidence associated with the values of the unknown parameters, in this case chronometric measurements, after the observation of the prior information. Details about the data and structure of comprehensive model for the dating of the PYS sequence was described previously[6].

Here we update the model by adding the new OSL age obtain for the burial infill (OSL4) and re-running the new model. We use OxCal 4.3.2[41], and the code is shown in Supplementary Information C. By inserting a "Date" command in the OxCal structure we allow the model to find the best fit for the age of the burial based on all OSL ages obtained for relevant Layers 17 and 18 (Supplementary Information C Table 4). Because of uncertainties in the bleaching history of sediment grains deriving from disturbed contexts, such as a burial, we do not tie the "Date" command to OSL4; instead we treat the burial infill sediment as another independent age for Layer 18.

Given that Layers 17 and 18 are statistically indistinguishable from each other and from OSL4, we may assume that both layers are quasi-contemporaneous, at least in the precision offered by the luminescence methods, for the studied period. The new model is shown in Extended Data Figure 1.

Screening for Ancient DNA

DNA extraction and library preparation. We screened for ancient DNA 8 undiagnosed skeletal fragments and 12 sediment samples associated with the PYS burial pit (Supplementary Information D Table 1). DNA was extracted from ~50mg of bone or sediment using a silica-based method developed for the retrieval of short DNA molecules[42] on an automated liquid handling platform[43]. 15% of each extract were converted into a single-stranded DNA library[44], and barcoded with a pair of unique indices[45], following the modifications described in Korlević et al. (2015)[46]. The number of DNA molecules incorporated into each library was assessed by quantitative PCR as described elsewhere[47]. Extraction and library negative controls were carried through all steps of the experiments. Libraries were pooled and shotgun sequenced on a HiSeq platform (Illumina).

Mitochondrial capture and sequencing. 1 µg of each amplified DNA library was enriched whether for mammalian mitochondrial DNA (mtDNA) using a probe set of 242 taxa[48] or for human mtDNA with a probe set covering the full human mitochondrial genome[49,50]. The enriched libraries were pooled in two sets according to the capture probe used and sequenced on a MiSeq platform (Illumina).

Sequence processing and mapping. The reads obtained from the sequencing of the mtDNA enriched libraries were trimmed to remove adapter sequences and overlapping paired-end reads were merged using leeHom[51]. Sequences from the mammalian mtDNA enriched libraries were aligned to a non-redundant database of 796 mammalian mitochondrial genomes from the NCBI Reference Sequence database (RefSeq) using nucleotide BLAST (BlastN)[52] with default parameters. Sequences were then assigned to different taxa using MEGAN[53] and each ancient taxon is deemed present in the dataset according to the requirement described earlier[54]. The sequences from the human mtDNA enriched libraries were aligned to the revised Cambridge Reference mitochondrial genome (rCRS, NC_0120920) using the Burrows-Wheeler Aligner (BWA)[55] with optimized parameters for ancient DNA «-n 0.01 –o 2 –l 16500»[56]. Aligned sequences shorter than 35 bases with a mapping quality lower than 25 were filtered out. PCR duplicates were removed by merging sequences with identical alignment start and end coordinates using bam-rmdup (https://github.com/mpieva/biohazard-tools).

Virtual reconstruction

PYS was recovered encased in a block and had to be manually and mechanically prepared for study. Given the delicate preservation and the infantile age stage of the specimen, a microCT scan was performed to extract digital 3D models of the teeth and bones, which were still embedded within the sediment. Because of the delicate state of preservation and the need of preserving the information regarding the position of the body a combination of mechanical and virtual isolation of the skeleton was decided. However, the low density of the bones prevented a proper virtual isolation of the elements, and it was necessary to carefully isolate the cranial from the postcranial elements (Supplementary Information A) and to combine microCT and surface scanners to reconstruct the original position of the child inside the block. The microCT scans were performed at the Laboratory of Microscopy of the Centro Nacional de

Investigacion sobre la Evolucion Humana–Unique Scientific & Technical Infrastuctures (CENIEH–ICTS, Burgos, Spain) with a Phoenix v|tome|x s (GE Measurement & Control). First, the entire block was scanned at 140 kV and 400 μA, with a 0.2 mm Cu filter and an integration time of 333 ms, resulting in an isometric voxel size of 0.1227 mm. As the remains were carefully manually cleaned, we performed a microCT of the block containing the cranial remains at 200 Kv and 400 μA, with the same filter and integration time, resulting in an isometric voxel size of 0.0769 mm, and another scan of the block containing the postcranial elements at 140kV and 250 μA, with the same filter and integration time, resulting in an isometric voxel size of 0.0479 mm. Each isolated tooth as well each smaller block resulting from the mechanical excavation were also microCT scanned. Additionally, surface scanners with a hand scanner (Artec Space Spider) under conditions of artificial light were performed of each excavated element and processed with Artec Studio 11 software to create surface models. Digital cleaning and segmentation was performed with Mimics 18.0 (Materialise, Be) and Avizo 7.0 (Visualization Sciences Group, 2012) using a combination of automatic and manual segmentation, generating STL files of all PYS remains. Digital renderings of the specimen in several views were done with Avizo, Mimics and MeshLab, respectively. With the digital renders, it was possible to identify several anatomical elements, such as the first vertebrae in anatomical connection. The identification of two teeth and several shells in the first microCT of the main block was useful as reference landmarks to later orient the microCT of the skull and the CT and surface scanner of the thorax in their original position. Furthermore, and to understand the position of the child within the block, the skull of a *Homo sapiens* child in a similar stage of development was microCT scanned and virtually reconstructed. Using Mimics and MeshLab software, both PYS and *Homo sapiens* crania were superimposed with the registration and align tool. A best-fit was made to reference them in the best position and see which parts were deformed or displaced. Furthermore, both crania were placed again in the burial pit using as a reference the 2 teeth identified in the first microCT scan of the main block. In addition, a comparative human skeleton of *H. sapiens* of similar age was scanned using the same surface scanner to obtain the digital models of all the long bones, hips and ribs, to help reconstruct the original position of the child inside the burial. Using Mimics software, all the models were scaled to obtain a length similar to that of a 2.5-3 year old (following Scheuer and Black, 2000[57]). To align the comparative skeleton with the PYS remains, the STL models of the vertebral column, ribs, clavicle, scapula and humerus were aligned using both the CT of the entire block and the CT of the PYS vertebral column.

Once all the remains and comparative models were aligned, 3ds Max 2020 (Autodesk) was employed combing the topopgraphic information available from the field, photographs of the excavation plan, all the STL and OBJ models of both Mtoto and the comparative skeleton to produce the closest reconstruction of the original position of the child when it was found at the siate. Each anatomical element was reoriented following the topographic field information and the orthophotos of the site. When all the remains were located in space, we proceeded to create textures, shadows and lights, to visualize the preserved skeletal elements and to integrate them in their original position in the comparative skeleton. Some renderings have been made with the semi-transparent comparative skeleton, to understand and visualize the position of the PYS into the burial, and understand its anatomical connection.

Thin section micromorphology and bone microscopy

A micromorphology sample collected at the end of the 2013 field season (PYS 2013_M1:19/18) intercepted soft, degraded bone. This sample was not processed for micromorphological analysis: it was stored until 2019, when it became apparent that it may have contained parts of Mtoto's skeleton (probably fragments of lower limbs and ribs). The box was then excavated at CENIEH (Burgos). Centimetre-sized bone fragments and lumps of the sediment matrix were collected for microscopic investigation, the results of which are reported here. The 2013 micromorphology sample was taken in a 6x10cm polyurethane box. Prior to its excavation at CENIEH, it had been stored at room temperature for 5.5 years. Human bone fragments and sediment lumps between the bones were collected on excavation of the sample box in 2019. Bone and sediment were air dried and impregnated with polyester resin under desiccation vacuum. One uncovered petrographic thin section (30µm thick) was produced from the impregnated block. The section was examined under a polarizing microscope (x10 to x400) at plane polarized (PPL), cross-polarized (XPL) and oblique incident light (OIL). Description of sediment features follows Bullock et al. (1985)[58], Stoops (2003)[59] and Stoops et al. (2018)[60]. Estimates and measurements of sediment inclusions and histological attributes of the bone fragments were made with the aid of standard semi-quantitative estimation charts and the *analySIS pro5* image analysis software. The degree of diagenetic alteration of bone was estimated mainly through optical microscopy, using the General Histology Index (GHI: Hollund et al. 2012[61]) – an estimate of microstructural alteration similar to the more commonly used Oxford Histology Index (OHI: Hedges et al. 1995[62]; Millard 2001[63]), but taking into account other types of structural and compositional alteration (generalised destruction, staining, accumulation of authigenic deposits, fissuring) besides bioerosion. Where identifiable, microscopic bioerosion ("*microscopical focal destruction*" – MFD: Hackett (1981)[64] was recorded following the typology proposed by Hackett (1981)[64] and Jans (2008)[17]. SEM-EDS analysis (on a Zeiss EVO-MA15, with an Oxford Instruments InCA Max 80 mm EDS) was carried out on the polished, uncoated thin section, to observe bone microstructure at higher magnifications and determine elemental composition of selected features. Low-vacuum conditions were used (60 Pa) to prevent charging of the sample surface; strict operating conditions of 50 μA filament current, 2.525 A gun current, 20 kV accelerating voltage, and an 8.5 mm working distance to achieve an acquisition rate of 15 kcps, were applied to standardise the analyses. A polished Co standard was analysed to adjust for beam current drift, and a polished dolomite standard was used to confirm the accuracy of the calculated absolute element concentrations. Navigation on the sample was aided by section scans. Data are reported as non-normalised percentage weights.

Dental analysis

Comparative metrical and morphological study of teeth. The evaluation of morphological features was made on the original fossils and the virtual images obtained by microtomography. The descriptive terminology used in this report derives from the following sources: Carlsen 1987[65], Tobias 1991[66], Turner et al. 1991[67], Scott and Turner 1997[68], Martinón-Torres et al. 2007[69], Martinón-Torres et al. 2008[70], Martínez de Pinillos et al. 2017[71], and Table 4 in Martinón-Torres et al. 2012[72], which includes a modified version of the Arizona State University Dental Anthropological System (ASUDAS) of scoring. Occlusal wear was recorded following Molnar 1971[73]. The comparison was focused in the Late Pleistocene samples, *H. sapiens* and *H. neanderthalensis*, although several samples from the Middle to late Pleistocene Africa were included in order to assess the variability of the African fossil record. The mesiodistal (MD) and buccolingual (BL) dimensions of the PYS child were measured by JMBC to the nearest 0.1 mm, following the methods of Flechier, Lefêvre, and Verdéne (1973)[74]. Apart from the MD and the BL, we have also calculated the computed crown area (CCA: MD X BL) and the measured crown area (CI: [BL/MD] x 100). In addition, the cusp areas of the M1s were measured following Bermúdez de Castro et al. (2001)[75] and using the criteria outlined by Bailey (2004)[76]. The areas were measured three times and the average of the three values was used. The total crown base area (TCBA) was calculated as the sum of all the individual cusp areas. The PYS values were compared against a large hominin sample of *H. sapiens*, *H. neanderthalensis* and some relevant Middle to Late Pleistocene fossils from Africa.

Enamel Thickness. Virtual sectioning of the molars was performed following the protocol described in Olejniczak and colleagues (2008)[77]. The mCT image stack was imported into Amira (6.3.0, FEI Inc.) and rotated into anatomical position. Then, the tip of three dentine horns (protoconid, metaconid and hypoconid in the mandibular molars and protocone, paracone and hypocone in the maxillary molars) were identified and the image stack was adjusted to intersect these three points of interest. A new plane perpendicular to the plane containing the three dentine horns was rotated to pass through the mesial dentine horns (protoconid and metaconid in the mandibular molars and protocone and paracone in the maxillary molars). We assessed enamel thickness from virtual 2D mesial cross-section planes in each PYS molar as described in Martin (1985)[78] using Amira (6.2, FEI Inc.) and ImageJ (1.51, NIH). In each mesial plane, we measured the enamel (c) and dentine cap (b, including the pulp) areas (in mm^2), adding up into the total crown area (a, in mm^2), and the enamel-dentine junction (EDJ) length (d, in mm). We calculated the average enamel thickness (AET=c/d), the relative enamel thickness ($RET= 100*AET/(b^{1/2})$) and the percentage of dentine and pulp in the molar crown (b/a=100*b/a in %). We assessed volume enamel thickness of the molar caps in the complete sample from PYS. Using Amira (6.3.0, FEI Inc.) we performed the segmentation of the dental tissues (enamel, dentine and pulp). We used the semiautomatic tool, threshold-based segmentation, and manual corrections. We employed the protocol of Olejniczak et al. (2008)[77] for the definition of the cervical plane. That is, the plane halfway between the most apical continuous ring of enamel and the plane containing the last hint of enamel. The following variables were measured and/or calculated: volume of the enamel (Ve in mm3); volume of the coronal dentine including the pulp enclosed in the crown (Vcdp in mm3); total volume of the crown, including the enamel, dentine and pulp (Vc in mm3); surface of the EDJ (SEDJ in mm2); percentage of dentine and pulp in the total crown volume (Vcdp/Vc =100*Vcdp/Vc in %); 3D average enamel thickness (3D AET=Ve/SEDJ in mm) and, 3D relative enamel thickness (3D RET=100*3D AET/(Vcdp1/3) a scale-free measurement)[77,79]. In order to extract the largest amount of information of the PYs specimens and the comparative sample, including the occlusal worn molars, we assessed lateral (non-occlusal) enamel thickness in the complete sample. In Amira (6.3.0, FEI Inc.) we defined the occlusal basin plane, a plane parallel to the cervical plane and tangent to the lowest enamel point of the occlusal basin. All material above the occlusal basin plane was removed and only the enamel, dentine and pulp between these two planes were measured[80,81]. The following variables were measured and/or calculated: lateral volume of the enamel (LVe in mm3); lateral volume of the coronal dentine including the pulp enclosed in the crown (LVcdp in mm3); total lateral volume of the crown, including the lateral enamel, dentine and pulp (LVc in mm3); lateral surface of the EDJ (LSEDJ in mm2); percentage of dentine and pulp in the lateral crown volume (LVcdp/LVc=100*LVcdp/LVc in %); 3D average enamel thickness (3D

LAET=LVe/LSEDJ in mm) and, 3D lateral relative enamel thickness (3D LRET=100*3D LAET/(LVcdp1/3) a scale-free measurement)[82]. The results of the 2D and 3D measurements in PYS specimens were compared with two populations, Neanderthals and modern humans (MH). Adjusted Z-scores[83,84] of the three variables accounting for tissue proportions (percentage of dentine, AET and RET) were computed to compare 2D and 3D values of the PYS specimens to the means and standard deviations of the Neanderthal and MH groups. This statistical method allows the comparison of unbalanced samples by using Student's inverse t distribution. In these Z-scores the -1.0 to +1.0 interval comprises the 95% of the variation in the reference sample. In addition, standard box and whisker plots were computed to represent three set of variables of crown volume and lateral volume (including 3D Vcdp/Vc, 3D AET, 3D RET and 3D LVcdp/Vc, 3D LAET, 3D LRET) in the PYS sample and the complete comparative specimens and/or groups.

Tissue distribution (cartographic maps). In order to visualize enamel thickness topographic distribution in PYS specimens, 3D chromatic maps were generated in Amira (6.3.0, FEI Inc.). The defined chromatic scale is from thinnest (blue) to thickest (red)[85,86]. For comparative purposes, we generated the chromatic maps of a selected sample of specimens, including: Neanderthals from Roc de Marsal (lower and upper deciduous m2), La Quina (upper permanent M1) and Abri Suard (lower permanent M1). Fossil *H. sapiens* from La Madaleine (lower deciduous m2), Qafzeh (upper deciduous m2 and upper and lower permanent M1). And, modern humans from European origin (upper and lower deciduous m2, and upper and lower permanent M1).

Geometric morphometric of the EDJ. We performed the Geometric morphometric (GM) analysis of the EDJ morphology on the virtual surfaces of PYS specimens and a comparative sample that included Neanderthals, fossil *H. sapiens* and modern humans

(Supplementary Information F Table 4). We reconstructed the slightly worn dentine horns of the comparative sample in Geomagic Studio (version 2012; www.geomagic.com) with the fill-holes tool. When necessary we mirrored the comparative specimens according to the PYS molar type. Using landmark tool in Amira, we placed one landmark on the dentine horn tip of each main cusp (protocone, paracone, metacone and hypocone on maxillary molars, and protoconid, metaconid, hypoconid, entoconid and hypocunulid on mandibular molars). Following, we placed a set of semilandmarks (96 and 95 points in maxillary and mandibular molars respectively) along the marginal crests. In each molar, configuration segments were saved independently. Using the package R, we generated the document containing the coordinate configuration for each molar type. Following, using R package we performed the weighted between-group principal component analysis (bgPCA) based on the Procrustes and deformation-based shape residuals[87]. Finally, we tested for allometry on the landmark-based analyses using the coefficient of determination (R2) of a multiple regression[88], in which the explicative variable is the centroid size and the dependent variables are the bgPC scores[89].

Faunal analysis

Zooarchaeology

Two separate zooarchaeological studies were conducted: N.A. analysed remains from burial fill at the Max Planck Institute for the Science of Human History in Jena, and M.E.P. analysed remains from Trenches 3-4 at the National Museums of Kenya in Nairobi. Access to comparative skeletal material for eastern Africa was distinct in each study, and analytical protocols differed somewhat.

Fauna, burial fill. For the burial fill (context 809 in Trench 8), all bone fragments were sorted, counted and measured (length, width and thickness) using a digital caliper (Mitutoyo 500–463), regardless of identifiability. The specimens were recorded in detail using codes following a zonation system that allow for the description of fragmentation patterns. All identified fragments were examined for bone surface modifications under a Nikon C-PCN stereomicroscope.

Fauna, Trenches 3-4. For Trenches 3-4, faunal remains are reported from the following layers and contexts: Layer 17 (contexts 316X, 317Y-Z, 420B-F), Layer 18 (422A-C), Layer 19 (423A-D). These remains were weighed and sorted into those identifiable at least to a minimal level (e.g., mammal limb bone), and those not easily identifiable at any level. For each identified specimen, recorded variables include taxon, element, portion, side, weathering, breakage, and bone surface modifications. Cortical surfaces of all identified specimens were examined with a 20x hand lens under strong oblique light.

Sediment analysis

Two sets of samples were analysed in the framework of this study. The first set comprises sediment samples from archaeological layers and the burial pit. The second set includes reddish micro-agglomerates associated with the child remains.

Sediment analysis from archaeological layers and the burial pit. Two groups of sediment samples were analysed. The first group comprises twenty-four samples of sediment collected during the excavation of Trenches 3 and 8 in 2017 (PYS-2017-200127 to PYS-2017-200153). They come from layers 17, 18 and 19, and were collected at 2 cm depth interval. They do not include sediment from the burial (Supplementary Information G Table 1).

The second group comprises five sediment samples collected close to the human remains (Supplementary Information G Table 2). Three samples, reddish-brown in colour, were retrieved close to the maxilla, the face, and inside the cranial vault. The other two, brownish in colour, were collected close to the occipital bone and the postcranial perimeter. These five samples were retrieved during the excavation of the skeleton at the CENIEH's Conservation and Restoration Laboratory.

The sediments samples were studied at the UMR 5199 PACEA and UMR 5060 IRAMAT/CRP2A laboratories in Bordeaux, France. The samples were examined and photographed with a motorised Leica Z6 APOA microscope equipped with a DFC420 digital camera. Uploaded images were treated with Leica Application Suite (LAS) equipped with the Multifocus module. Samples were then prepared for grain-size analysis with a Horiba LA-950 laser particle size analyser. The sample pre-treatment included suspension in sodium hexametaphosphate (5 g/l) and hydrogen peroxide (35%) at room temperature for 12 h. The resulting compound was subjected to 60 s ultrasonification to achieve optimal dispersion. The Mie solution to Maxwell's equation provided the basis for calculating the particle size[90,91], using a refractive index of 1.333 for water and 1.55 – 0.01i for the particles. The grain-size distributions expressed in ϕ units were decomposed in different Gaussian populations (parametric curve fitting method) using the mixdist R package[92] to identify the main modes and their relative proportions. The limits used for grain-size classes are as follows: <7 μm (clays), 7–63 μm (silts), 63-2000 μm (sands). They are based on studies showing that the amount of clay particles measured by laser diffraction is usually underestimated (e.g. Konert and Vandenberghe, 1997[93]).

Elemental analysis was carried out by using a hand-held SPECTRO xSORT energy dispersive X-ray fluorescence (EDXRF) spectrometer from Ametek. This instrument is equipped with a silicon drift detector (SDD), a low power W X-ray tube with an excitation source of 40 kV, and an X-ray beam of 8 mm. Spectra acquisition times were set to 300 s. Measurements were performed with a constant working distance by using a positioning device consisting of a lead receptacle to which the spectrometer was fixed. Samples were previously ground and homogenized with an agate mortar and then placed into a plastic cup covered with a Prolene® thin film. Three measurements were taken on each sample. Element contents were calculated as the average of these acquisitions. In order to precisely quantify the elemental composition of the samples a dedicated calibration for sediment samples was applied (see Sitzia et al., 2019[94] for details). This calibration allows quantifying Si, K, Ca, Ti, V, Cr, Mn, Fe, Ni, Zn, Ga, As, Rb, Sr, Y, Zr, and Ba. Centred log ratio (*clr*) was used to analyse geochemical data as an alternative to the raw percentages, following Aitchison (1986)[95]. Prior to statistical analysis, a non-parametric replacement was made for the null values below the limit of detection, according to the method proposed by Martín-Fernández et al. (2003)[96]. Some elements were excluded when they displayed more than one third of missing values (Cr, Ni, Sr) or showed a heterogeneous distribution (V). We performed principal component analysis (PCA) of EDXRF concentrations for the thirteen major, minor, and trace elements more frequently detected (Si, K, Ca, Ti, Mn, Fe, Zn, Ga, As, Rb, Y, Zr, Ba). All data analyses were done with the *ade4* package[97] for R software.

We performed XRD analyses on powder samples by using a Bruker D8 Advance diffractometer (Bragg-Brentano Theta-Theta geometry, fixed sample in the horizontal plane, movable tube and detector), goniometer diameter 600mm, Cu anti-cathode X source, Cu-Kα incident X incident doublet radiation. Acquisitions were conducted with an angular range of 3-60° at 2Θ (reticular distances 1.54-29 Å), measurement step 0.01°, a 181px linear detector type Bruker LynxEye covering simultaneously 2.6 ° in

2Θ, an analysis time per point of 550 s (approx. 9 min/px), an angular reproducibility of 0.017°, supporting samples holders of 25 mm in diameter and 1.5 mm thickness, made of PolyMethyl MethAcrylate (PMMA) holders. Samples were previously ground and homogenized with an agate mortar. The time of analysis was 5 h. Mineralogical phases and the semi-quantitative analysis were achieved by using the routine DIFFRAC.SUITE™ EVA software package (Bruker AXS GmbH, Germany) which allows mathematical deletion of bottom noise and Cu-Kα2 component, combined with the specific powder diffraction file (PDF2) database (International Centre for Diffraction Data—ICDD, Pennsylvania, USA).

Reddish micro-agglomerates associated with the child remains

The reddish micro-agglomerates, possibly fragments of iron-rich rocks commonly called ochre, were detected in the sediment coating the child remains during their excavation and consolidation at the CENIEH. An analytical pipeline involving observation and sampling under low-magnification optical microscope, Raman spectroscopy, X-ray Diffraction (XRD) and Scanning Electron Microscopy coupled with Energy Dispersive X-Ray Spectroscopy (SEM-EDS), was applied to establish the elemental and mineralogical composition of these micro-agglomerates. The aim was to investigate whether ochre may have been involved in the mortuary practices that have led to the deposition and preservation of the child remains. All analyses were conducted at the CENIEH Archaeometry and Microscopy laboratories.

Two groups of reddish micro-agglomerates were analysed. The first set consists of 55 micro-agglomerates contained in samples of reddish-brown clay sediment collected close to the maxillary, the face, and inside the cranial vault. The micro-agglomerates typically correspond to ~900x600 µm associations of grains featuring distinct reddish shades (Supplementary Information G Figure 1). The second group is composed of two larger –~2-10 mm– red fragments collected on the ribs and vertebral bodies (Supplementary Information G Figure 2). Fifteen agglomerates from the first group and the two composing the second group were submitted to analytical microscopy (Raman spectroscopy, SEM-EDS) and XRD analysis (Supplementary Information G Table 3).

A FEI Quanta 600 SEM fitted with EDS, and Oxford Instruments INCA software to interface with the EDS, was used to obtain an estimation of the bulk elemental composition of the agglomerates. Operating conditions were 15kV of acceleration voltage, working distance of 10 mm, and acquisition time of 90 seconds, resulting in typical dead times between 10 and 17 %. Unless otherwise specified, results are given as compound weight %, oxygen calculated by stoichiometry and normalised to 100%. All SEM micrographs are Low Vacuum Secondary Electron (SE) images.

The samples were first observed at low magnification – typically ranging 100-200x – to capture the entire particle (Supplementary Information G Figure 3). Three representative locations were then selected to investigate the samples microstructure at 1200x where surface features and mineral phases were measured. Three areas were analysed at each location to estimate the average bulk chemical composition. Finally, a mapping of the matrix between crystals was conducted at 2400x and compared to the bulk composition obtained at 1200x (Supplementary Information G Figure 4). Occasionally, other magnifications were used to better investigate texture, grain morphology and their relation with elemental composition. Analyses at high magnifications were conducted to avoid potential biases due to surface irregularities and voids. The analytical procedure was adapted from the analysis of similar mineral particles described in Pitarch Martí et al. (2017)[98].

The mineralogical composition of the sample was established by XRD. Due to the destructive nature of this technique, these analyses were not performed on agglomerates analysed by SEM-EDS and RAMAN but on residues coming from the same samples. Sediment was hand grounded in an agate mortar with a pestle. The resulting powder was tapped on silicon discs and mounted into stainless steel sample holders. Patterns were collected with a PANalytical X´Pert PRO MPD diffractometer with CuKα radiation (λ=1.5406 Å) and a solid-state multichannel detector. Each sample was scanned over the 2-theta range 5- 80˚ with a step size of 0.03. The working tension and intensity were 45kV and 40mA respectively, and the time of analysis ranged from 3 to 16 h. Semi-quantitative analysis was performed on the XRD data using the X´Pert High Score software. Due to the small amount of material analysed the results should be regarded as qualitative.

Raman spectra were acquired using a DRX Thermo Scientific Raman dispersive spectrometer, with a laser emitting at 780 nm. The power radiation measured under the Olympus x50 microscope objective was about 0.5 mW-0.8 mW. Acquisitions of about 25 seconds and multiple additions were used. The spectrometer worked in a spectral range from 55 to 3350 cm^{-1}. The calibration of the spectrometer was done with a polystyrene standard (main band: 1000 cm^{-1}). The recorded mineral spectra were contrasted against the RRUFF database library for phase identification[99] as well as Julien et al. (2004)[100], Bellot-Gurlet et al. (2009)[101], Hanesch (2009)[102] and Babay et al. (2015)[103].

41. Bronk Ramsey, C. Bayesian analysis of radiocarbon dates. *Radiocarbon* **51**, 337–360 (2009).
42. Dabney, J. *et al.* Complete mitochondrial genome sequence of a Middle Pleistocene cave bear reconstructed from ultrashort DNA fragments. *Proc. Natl. Acad. Sci.* **110**, 15758–15763 (2013).

43. Rohland, N., Glocke, I., Aximu-Petri, A. & Meyer, M. Extraction of highly degraded DNA from ancient bones, teeth and sediments for high-throughput sequencing. *Nat. Protoc.* **13**, 2447–2461 (2018).
44. Gansauge, M.-T. *et al.* Single-stranded DNA library preparation from highly degraded DNA using t4 DNA ligase. *Nucleic Acids Res.* **45**, e79 (2017).
45. Kircher, M., Sawyer, S. & Meyer, M. Double indexing overcomes inaccuracies in multiplex sequencing on the Illumina platform. *Nucleic Acids Res.* **40**, e3 (2012).
46. Korlević, P. *et al.* Reducing microbial and human contamination in DNA extractions from ancient bones and teeth. *BioTechniques* **59**, 87–93 (2015).
47. Glocke, I. & Meyer, M. Extending the spectrum of DNA sequences retrieved from ancient bones and teeth. *Genome Res.* **27**, 1230–1237 (2017).
48. Slon, V. *et al.* Mammalian mitochondrial capture, a tool for rapid screening of DNA preservation in faunal and undiagnostic remains, and its application to Middle Pleistocene specimens from Qesem Cave (Israel). *Quat. Int.* **398**, 210–218 (2015).
49. Maricic, T., Whitten, M. & Pääbo, S. Multiplexed DNA sequence capture of mitochondrial genomes using PCR products. *PLoS One* **5**, e14004 (2010).
50. Fu, Q. *et al.* DNA analysis of an early modern human from Tianyuan Cave, China. *Proc. Natl. Acad. Sci.* **110**, 2223–2227 (2013).
51. Renaud, G., Stenzel, U. & Kelso, J. leehom: adaptor trimming and merging for illumina sequencing reads. *Nucleic Acids Res.* **42**, e141 (2014).
52. Altschul, S. F., Gish, W., Miller, W., Myers, E. W. & Lipman, D. J. Basic local alignment search tool. *J. Mol. Biol.* **215**, 403–410 (1990).

53. Huson, D. H., Auch, A. F., Qi, J. & Schuster, S. C. MEGAN analysis of metagenomic data. *Genome Res.* **17**, 377–386 (2007).

54. Slon, V. *et al.* Neandertal and Denisovan DNA from Pleistocene sediments. *Science* **356**, 605–608 (2017).

55. Li, H. & Durbin, R. Fast and accurate short read alignment with Burrows-Wheeler transform. *Bioinformatics* **25**, 1754–1760 (2009).

56. Meyer, M. *et al.* A high-coverage genome sequence from an archaic Denisovan individual. *Science* **338**, 222–226 (2012).

57. Scheuer, L. & Black, S. Development and ageing of the juvenile skeleton. in *Human Osteology: In Archeology and Forensic Science* (eds. Cox, M. & Mays, S.) 9–22 (Cambridge University Press, 2000).

58. Bullock, P. *et al. Handbook for Soil Thin Section Description*. (Waine Research, 1985).

59. Stoops, G. *Guidelines for Analysis and Description of Soil and Regolith Thin Sections*. (Soil Science Society of America, 2003).

60. *Interpretation of Micromorphological Features of Soils and Regoliths*. (Elsevier, 2018).

61. Hollund, H. I. *et al.* What happened here? Bone histology as a tool in decoding the postmortem histories of archaeological bone from Castricum, the Netherlands. *Int. J. Osteoarchaeol.* **22**, 537–548 (2012).

62. Hedges, R. E. M., Millard, A. R. & Pike, A. W. G. Measurements and relationships of diagenetic alteration of bone from three archaeological sites. *J. Archeol. Sci.* **22**, 201–209 (1995).

63. Millard, A. R. The deterioration of bone. in *Handbook of Archaeological Sciences* (eds. Brothwell, D. R. & Pollard, A. M.) 637–674 (Wiley, 2001).

64. Hackett, C. J. Microscopical focal destruction (tunnels) in exhumed human bones. *Med. Sci. Law* **21**, 243–265 (1981).
65. Carlsen, O. *Dental Morphology*. (Munksgaard, 1987).
66. Tobias, P. V. *The Skulls, Endocasts and Teeth of Homo habilis*. vol. 4 (Cambridge University Press, 1991).
67. Turner, C. G., Nichol, C. R. & Scott, G. R. Scoring procedures for key morphological traits of the permanent dentition: the Arizona State University dental Anthropology System. in *Advances in Dental Anthropology* (eds. Kelley, M. & Larsen, C.) 13–31 (Wiley-Liss, 1991).
68. Scott, G. R. & Turner, C. G. *The Anthropology of Modern Human Teeth: Dental Morphology and Its Variation in Recent Human Populations*. (Cambridge University Press, 1997).
69. Martinón-Torres, M. *et al.* Dental evidence on the hominin dispersals during the Pleistocene. *Proc. Natl. Acad. Sci.* **104**, 13279–13282 (2007).
70. Martinón-Torres, M. *et al.* Dental remains from Dmanisi (Republic of Georgia): morphological analysis and comparative study. *J. Hum. Evol.* **55**, 249–273 (2008).
71. Martínez de Pinillos, M., Martinón-Torres, M., Martín-Francés, L., Arsuaga, J. L. & Bermúdez de Castro, J. M. Comparative analysis of the trigonid crests patterns in Homo antecessor molars at the enamel and dentine surfaces. *Quat. Int.* **433**, 189–198 (2017).
72. Martinón-Torres, M., Bermúdez de Castro, J. M., Gómez-Robles, A., Prado-Simón, L. & Arsuaga, J. L. Morphological description and comparison of the dental remains from Atapuerca-Sima de los Huesos site (Spain). *J. Hum. Evol.* **62**, 7–58 (2012).

73. Molnar, S. Human tooth wear, tooth function and cultural variability. *Am. J. Phys. Anthropol.* **34**, 175–190 (1971).

74. Lefêvre, J. Etude odontologique des hommes de Muge. *Bull. Mém. Soc. Anthropol. Paris* **10**, 301–333 (1973).

75. Bermúdez de Castro, J. M., Sarmiento, S., Cunha, E., Rosas, A. & Bastir, M. Dental size variation in the Atapuerca-SH Middle Pleistocene hominids. *J. Hum. Evol.* **41**, 195–209 (2001).

76. Bailey, S. E. A morphometric analysis of maxillary molar crowns of Middle-Late Pleistocene hominins. *J. Hum. Evol.* **47**, 183–198 (2004).

77. Olejniczak, A. J. *et al.* Dental tissue proportions and enamel thickness in Neandertal and modern human molars. *J. Hum. Evol.* **55**, 12–23 (2008).

78. Martin, L. Significance of enamel thickness in hominoid evolution. *Nature* **314**, 260–263 (1985).

79. Kono, R. T. Molar enamel thickness and distribution patterns in extant great apes and humans: new insights based on a 3-dimensional whole crown perspective. *Anthropol. Sci.* **112**, 121–146 (2004).

80. Toussaint, M. *et al.* The Neandertal lower right deciduous second molar from Trou de l'Abîme at Couvin, Belgium. *J. Hum. Evol.* **58**, 56–67 (2010).

81. Zanolli, C. *et al.* Is the deciduous/permanent molar enamel thickness ratio a taxon-specific indicator in extant and extinct hominids? *C. R. Palevol* **16**, 702–714 (2017).

82. Olejniczak, A. J. & Grine, F. E. High-resolution measurement of Neandertal tooth enamel thickness by microfocal computed-tomography. *S. Afr. J. Sci.* **101**, 219–220 (2005).

83. Maureille, B., Rougier, H., Houët, F. & Vandermeersch, B. Les dents inférieures du Néandertalien Regourdou 1 (site de Regourdou, commune de Montignac, Dordogne): analyses métriques et comparatives. *Paleo* **13**, 183–200 (2001).
84. Scolan, H., Santos, F., Tillier, A.-M., Maureille, B. & Quintard, A. Des nouveaux vestiges Néanderthaliens à Las Pélénos (Monsempron-Libos, Lot-et-Garonne, France). *Bull. Mém. Soc. Anthropol. Paris* **24**, 69–95 (2012).
85. Macchiarelli, R., Bondioli, L., Mazurier, A. & Zanolli, C. Virtual dentitions: touching the hidden evidence. in *Technique and Application in Dental Anthropology* (eds. Irish, J. D. & Nelson, G. C.) 425–448 (Cambridge University Press, 2008).
86. Bayle, P. *et al.* Three-dimensional imaging and quantitative characterisation of human fossil remains - examples from the NESPOS database. in *Pleistocene Databases: Acquisition, Storing, Sharing* (eds. Macchiarelli, R. & Weniger, G. C.) 29–46 (Mettmann: Wissenschaftliche Schriften des Neanderthal Museums 4, 2011).
87. Mitteroecker, P. & Bookstein, F. Linear discrimination, ordination, and the visualization of selection gradients in modern morphometrics. *Evol. Biol.* **38**, 100–114 (2011).
88. Bookstein, F. *Morphometric Tools for Landmark Data Geometric and Biology*. (Cambridge University Press, 1991).
89. Mitteroecker, P., Gunz, P., Windhager, S. & Schaefer, K. A brief review of shape, form, and allometry in geometric morphometrics, with applications to human facial morphology. *Hystrix* **24**, 59–66 (2013).
90. Jones, R. M. Particle size analysis by laser diffraction: ISO 13320, standard operating procedures, and mie theory. *Am. Lab.* **35**, 44–47 (2003).

91. ISO. *Particle size analysis - Laser diffraction methods, Part 1: General principles, Annex A: Theoretical background of laser diffraction*. (2009).
92. Macdonald, P. & Du, J. *Mixdist: Finite mixture distribution models*. (2012).
93. Konert, M. & Vandenberghe, J. Comparison of laser grain size analysis with pipette and sieve analysis: A solution for the underestimation of the clay fraction. *Sedimentology* **44**, 523–535 (1997).
94. Sitzia, L., Gayo, E. M. & de Pol-Holz, R. A perched, high-elevation wetland complex in the Atacama Desert (northern Chile) and its implications for past human settlement. *Quaternary Research* **92**, 33–52 (2019).
95. Aitchison, J. *The Statistical Analysis of Compositional Data*. (Chapman and Hall, 1986).
96. Martín-Fernández, J. A., Barcelo-Vidal, C. & Pawlowsky-Glahn, V. Dealing with zeros and missing values in compositional data sets using nonparametric imputation. *Math. Geol.* **35**, 253–278 (2003).
97. Dray, S. & Dufour, A.-B. The ade4 package: Implementing the duality diagram for ecologists. *J. Stat. Soft.* **22**, (2007).
98. Pitarch Martí, A., Wei, Y., Gao, X., Chen, F. & d'Errico, F. The earliest evidence of coloured ornaments in china: The ochred ostrich eggshell beads from Shuidonggou Locality 2. *J. Anthropol. Archaeol.* **48**, 102–113 (2017).
99. Downs, R. T. The RRUFF project: An integrated study of the chemistry, crystallography, raman and infrared spectroscopy of minerals. in (2006).
100. Julien, C. M., Massot, M. & Poinsignon, C. Lattice vibrations of manganese oxides. *Spectrochim. Acta A* **60**, 689–700 (2004).
101. Bellot-Gurlet, L. *et al.* Raman studies of corrosion layers formed on archaeological irons in various media. *J. Nano Res.* **8**, 147–156 (2009).

102. Hanesch, M. Raman spectroscopy of iron oxides and (oxy) hydroxides at low laser power and possible applications in environmental magnetic studies. *Geophys.* **177**, 941–948 (2009).

103. Babay, S., Mhiri, T. & Toumi, M. Synthesis, structural and spectroscopic characterizations of maghemite γ-Fe2o3 prepared by one-step coprecipitation route. *J. Mol.* **1085**, 286–293 (2015).

Acknowledgements Funding for this project was provided by the SEALINKS project under a European Research Council (ERC) grant (no. 206148) and by the Max Planck Society (to N.B.). Funding for the hominin analyses was from the Dirección General de Investigación of the Ministerio de Ciencia, Innovación y Universidades, grant numbers PGC2018-093925-B-C31 and C33 (MCI/AEI/FEDER, UE) and The Leakey Foundation, through the personal support of G. Getty (2013) and D. Crook (2014-2020) to M.M.-T.; analyses were also carried out at the laboratories of the CENIEH-ICTS with the support of the CENIEH staff. E.S. has a Ramón Areces/Atapuerca Foundation postdoctoral grant. L.M.F. is beneficiary of an Atapuerca Foundation postdoctoral grant. S.J.A. and F.D. acknowledge support from the Research Council of Norway, through its Centres of Excellence funding scheme, SFF Centre for Early Sapiens Behaviour (SapienCE) (no. 262618). FD was funded by the ERC grant, TRACSYMBOLS (no. 249587), the Agence Nationale de la Recherche (ANR-10-LABX-52), LaScArBx Cluster of Excellence, and the Talents program of the University of Bordeaux, *Initiative d'Excellence*. We thank Nick Blegen for conducting the digital work in the field and Rebeca García from University of Burgos for assisting in anatomical identifications. Permission to conduct the research was granted by the Office of the President of the Republic of Kenya through affiliation with the National

Museums of Kenya (NMK). We are also grateful for the support of the NMK and the British Institute in Eastern Africa.

Author contributions N.B., M.D.P and E.N. designed and directed the PYS field research; C.S. and J.B. conducted the field excavations; M.M.-T., J.M.B.C., J.L.A., E.S., L.M.F analysed the hominin fossil; P.F. conducted the mechanical restoration and conservation of the hominin; E.S. and J.G.G. conducted the virtual restoration and reconstruction of the hominin; F.d'E., N.A., W.A., S.J.A., J.B., A.C., S.D., K.D., F-X. LB., A.A., D.L., N.K., G.M., D.M., J.M., J.M.M. A.P.M., M.E.P., A.Q., S.R., P.R., M.J.S., C.S. and I.S. conducted analytical studies; M.M.-T., N.B. and M.D.P. wrote the paper with contributions of all authors.

Competing interests The authors declare no competing interests.

Additional information

Supplementary Information is available in the online version:

Correspondence and requests for materials should be addressed to M.M.-T., N.B. or M.D.P.

Extended Data Fig. 1. PYS MSA lithics. Above: The size distribution of flakes through Layers 18-17 (MSA) and Layer 16 (early LSA). Notice the decrease in size across Layers 17-16. The small sample of flakes recovered from the burial (n=14), shown here with a boxplot, falls within the variation in product weight for the MSA. Below: Facetted limestone flakes from MSA layers of PYS. A: limestone flake with facetted dihedral platform from burial context (809). B: Retouched limestone flake with large facetted platform from Layer 17.

Extended Data Fig. 2. Bayesian model for the age estimation of PYS. Left: Bayesian model of all available age determinations from PYS, produced using OxCal v4.4.2 and

IntCal20. Right: Age estimate of the burial determined using Bayesian model. A full description (OxCal code) of the age model is provided in Supplemental Information C.

Extended Data Fig. 3. Micromorphological and histological analysis. a, Ferruginous microfacies (MF-fer: here a coarser-grained variant) adhering on cancellous bone (plane polarised light: PPL). **b,** Sharp boundary between ferruginous (MF-fer) and carbonate microfacies (MF-carb) in sediment between Mtoto's bones (cross-polarised light: XPL). Angular ferruginous nodules and/or MF-fer intraclasts are present within the carbonate microfacies. **c,** Mtoto's bone fragment. A Fe oxide-stained calcite crust (Ca) covers the bone surface. A thin zone of non-clouded bone ('HAP' – conventionally 'hydroxyapatite') immediately beneath the bone surface is underlain with clouded, Ca-enriched bone of the mesosteum (CLb). Note the sharp boundary between HAP and CLb (especially at the left side), and dense bioerosion foci within CLb, such as the linear longitudinal tunnels; budding tunnels (dark spots) and enlarged osteocyte lacunae (smaller dark spots). Double arrow shows two possible Wedl tunnels. PPL. **d,** As in (c), but in XPL. Note that the calcite crust (Ca) comprises two layers: a Fe oxide-stained, microcrystalline layer, and a latter one, of clear, coarser-crystalline calcite (grey arrow). Birefringent areas within clouded bone (CLb) mark osteons. Note the loss of birefringence in bioerosion foci (e.g. lower right corner). **e,** Enlarged osteocyte canaliculi and lacunae in clouded, Ca-enriched bone. PPL. **f,** Advanced alteration of putative human bone (GHI: 2), with small areas of preserved histology, pervasive 'clouding', fissuring (e.g. blue arrow), dissolution pores (e.g. green arrow) and Fe and Mn impregnation (black spots). Note the spatial patterning of bioerosion, with domains of larger, circular coalescent non-Wedl MFD (e.g. red arrow) and smaller, more typical tunnels (budding and linear longitudinal: e.g. white arrow). A crust of calcite speleothem (grey arrows) encrusts a transverse fracture across the bone (PPL). **g,** Budding and linear longitudinal tunnels in highly altered bone (area marked with white arrow in (f). Some smaller-scale, spongiform bioerosion is also shown, surrounded with permineralised rims of redeposited ‘hypdoxyapatite’ (white bands). SEM image. **h,** Periosteum of clouded bone (Cb), encrusted with carbonate deposits (MF-carb). Note the irregular, pitted microrelief of the bone surface, indicative of dissolution. Larger circular-elliptical pores (blue/turquoise) are haversian canals. Circles show foci of fine-scale bacterial bioerosion within clouded bone. SEM image, with colour temperature filter to enhance resolution.

Extended Data Fig. 4. Histological analysis of Mtoto’s bone. Elemental composition of clouded bone (Cb) and encrusting carbonate sediment (Cc) (SEM-EDS image and spectra). The pictured area corresponds to that of Extended Data Figure 3 c,d. Diffuse lighter grey areas within the clouded bone may be perimineralised rims around bioerosion foci. Note the variable enrichment in Ca (especially in Spectrum 21) and the low concentrations of Fe, Al and Mg in the authigenic Ca-P phase that makes up clouded bone.

Extended Data Fig. 5. Reconstruction of key taphonomic events of Mtoto's burial. The 3D sequence (a,b,c) illustrates the reconstruction of the key taphonomic events affecting the shape and relationship of the head and the spine. **a**, Original right lateral decubitus position of the child in the burial pit. **b**, Lateral compression of the thorax because of the sediment weight; the ribs are flattened but the rib cage does not collapse as it is common in decomposition in filled space (earth grave). c, The head dislocates as it is typical in the case of burials with perishable head support. **d**, Ideal reconstruction of Mtoto's original position at the moment of its discovery at the site.

Extended Data Fig. 6. PYS Shell analysis. **a,** Fragments of *Achatina* cf. *fulica* found in close association with the child skeleton. Observation of anatomical features allows for a precise identification of the provenance of the shell fragments. Fragments PYS-2017-200407 and PYS-2017-200404 come from the area of the body whorl adjacent to the middle portion of the parietal callus. Fragment PYS-2017-200405 comes from a portion of the shell close to that of the previous fragment, and may derive from the same individual. Fragment PYS-2017-200406 comes from the middle of the body whorl, on its dorsal aspect. Although anatomically it is compatible with a provenance from the same individual, it is very dark in colour, suggestive of a higher Mn intake; additionally, the concretion coating its outer surface has a different texture, indicating that it had a different taphonomic history, possibly indicating it derives from a different shell. Fragment PYS-2017-200086.D comes from the middle of the body whorl, on its ventral aspect. **b,** Refitting of fragments PYS-2017-200407 and PYS-2017-200404. The two large fragments refit along an ancient fracture perpendicularly intercepting the shell growth lines. **c,** Modern striations on the inner surface of specimen PYS-2017-200406, probably produced during excavation or cleaning of the fragments. The modern origin of the striations is shown by their random orientation and absence of the thin manganese patina adhering on the inner surface of this specimen. **d,** Micrographs and 3D reconstruction of an area of fragment PYS-2017-200404 outer surface showing two grooves obliquely crossing the decussated sculpture of the outer shell surface. The grooves internal morphology and outline indicate that they were made by a pointed instrument, possibly a stone tool, following the irregular morphology of the shell natural surface and slightly changing direction when running into concave areas. The antiquity of the lines is demonstrated by the red sediment coating the specimen, which fills the striations and almost completely buries them when they run into natural grooves of the shell. **e,** Fragments of *Achatina* cf. *fulica* found in feature 809 (bottom) and their anatomical origin (top). The twelve fragments mostly come from the *Achatina* snail's body whorl and the last whorls of the spire; only two come from the parietal wall and the apex. They present a similar state of preservation, colour, taphonomic modifications and type of associated concretions with those observed on the five fragments found in direct association with the skeleton. None of these fragments bear incisions similar to those recorded on specimen PYS-2017-200404. Fragments comprising the control sample from Layer 18 are, in general, less frequently encrusted with concretions in comparison to those from the skeleton and the burial pit (809). **f,** Biplot correlating the length and width of *Achatina* cf. *fulica* fragments from the burial pit and associated skeleton in comparison to those from Layer 18 (L18) (top), and the length and width distributions of *Achatina* cf. *fulica* fragments form these two contexts (bottom). The fragments from the burial pit are significantly larger in size ($p = 0,001$) while displaying the same length/width ratio. Incorporation in the grave fill preserved *Achatina* fragments from greater levels of fragmentation in comparison to those in Layer 18, which may have been subject to trampling.

Extended Data Fig. 7. **PYS human dental tissue comparison. a**, Adjusted Z-scores of 2D and 3D, complete crown and lateral enamel, variables. Z-score graphs for the crown average enamel thickness (2D and 3D AET and 3D LAET), relative enamel thickness (2D and 3D RET and 3D LRET), and percentage of dentine and pulp (2D Acdp/Ac, 3D Vcdp/Vc and 3D LVcdp/LVc) in the three PYS molars in comparison with the variation expressed in Neanderthals (blue triangles) and recent modern humans (red circles). The solid line passing through zero represents the mean, and the -1 and 1 values correspond to the 95% limit of variation of the two comparative samples. **b**, Enamel thickness cartographies of the PYS upper and lower molars compared with those of extinct and extant specimens. Topographic thickness variation is rendered by a pseudo-colour scale ranging from thinner (dark-blue) to thicker (red). (O=occlusal, B=buccal). Ldm2 (first row): PYS, NEA=Neanderthal (Roc de Marsal), FHS=fossil *H. sapiens* (Qafzeh 10) and MH=modern human of European origin. RM1 (central row): PYS, NEA=Neanderthal (La Quina), FHS=fossil *H. sapiens* (Qafzeh 15) and MH=modern human of European origin. RM1 (central row): PYS, NEA=Neanderthal (Abri Suard), FHS=fossil *H. sapiens* (Qafzeh 15), and MH=modern human of European origin.

Extended Data Table 1. Diagenesis of identifiable and putative human bone in Mtoto's section. lld: linear-longitudinal MFD; bd: budded MFD; lam: lamellate MFD; HAP: hydroxyapatite; Cc: calcite.

Extended Data Table 2. PYS faunal remains. Fragmentation of the appendicular skeletal elements recorded from the fill close to the burial in Trench 8. The high level of fragmentation of the faunal remains contrasts with the relative completeness but advanced degradation of Mtoto's skeletal remains, indicating different taphonomic histories for faunal and human remains.

Figures

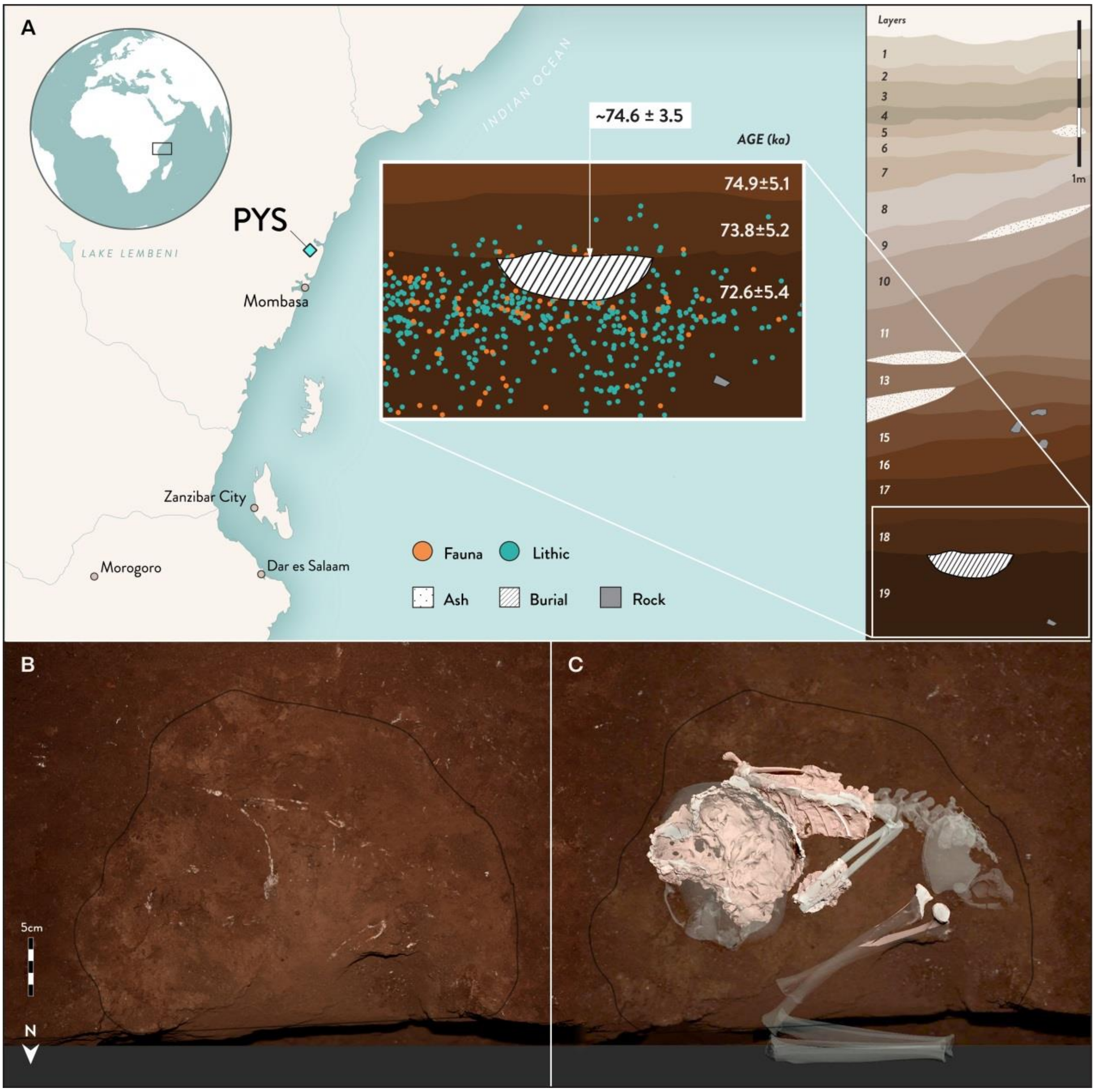

Fig. 1: Location of PYS and stratigraphic context of burial. **a**, PYS is located in the uplands of Kenya's coastal plain. Panel on right side shows the 19 stratigraphic layers with the location of burial pit in MSA Layer 19. Detailed inset of burial pit shows piece-plotted objects, including MSA lithics and fauna and three associated OSL dates in Layers 17-19. The Bayesian age is ~74.6 ± 3.5 ka. **b**, Plan view of the 2017 excavation. The black line delimits the pit feature and the change in texture from the surrounding matrix. The faint white outline of the decomposed skull, spine, femur and other severely degraded bones can be observed on the surface of the pit. **c**, Same view with the superimposition of the virtual reconstruction of the CT and surface scans of Mtoto. The preserved parts (solid) are superimposed over a semi-transparent comparative skeleton to better depict the position of the child.

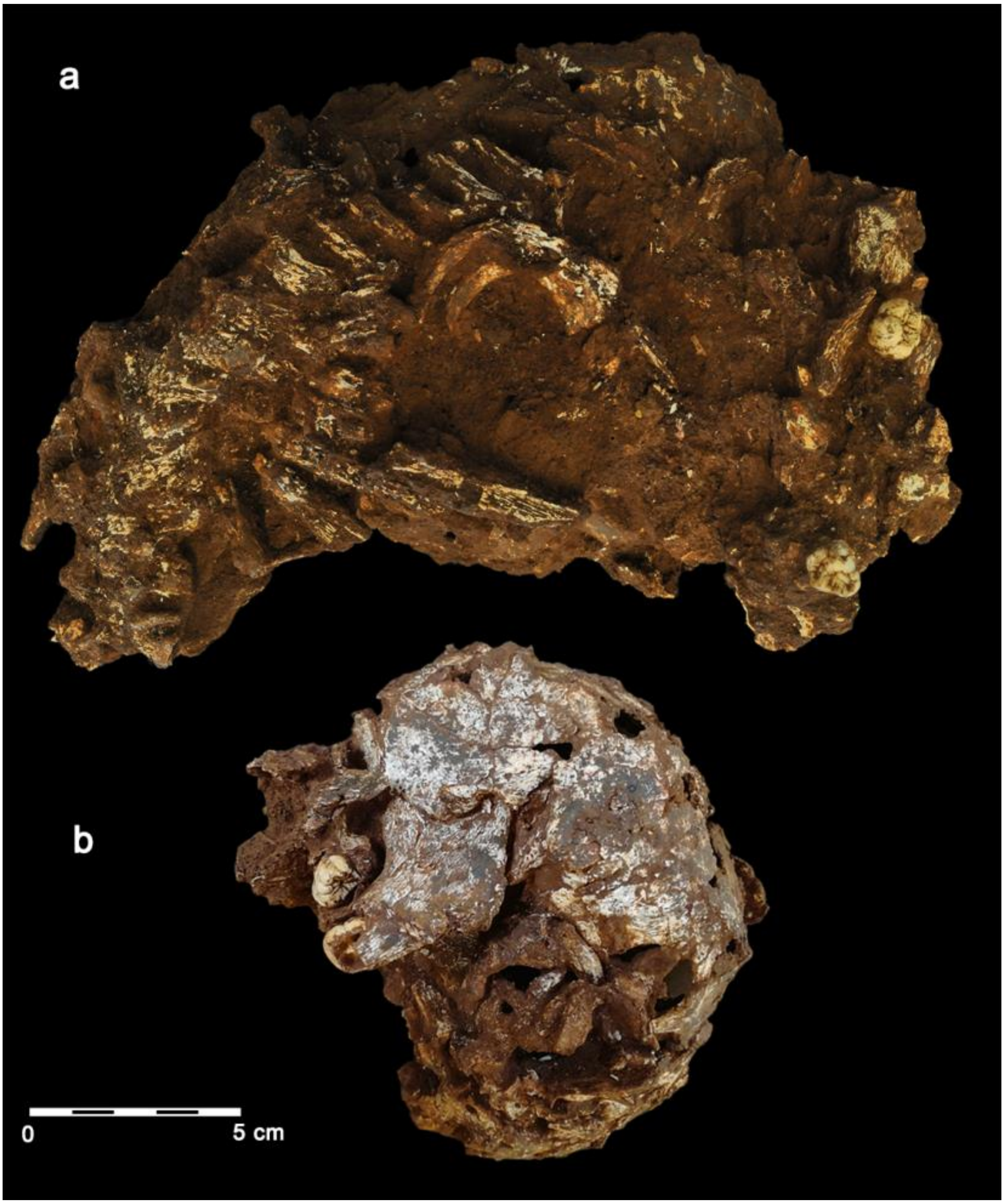

Fig. 2: PYS human fossil. **a**, External view of the PYS main block where the flexed spine with articulated vertebrae and ribs, as well as some teeth are partially exposed on the surface. The photograph was taken after the initial cleaning and removal of three right thoracic ribs, which revealed how the first and second ribs descended and rotated into the thoracic cavity while preserving the intercostal space. This argues in favour of minimal displacement of this part of the body as a unit given the sternal articulation of the pectoral girdle. **b**, External view of the left side of Mtoto's skull and left hemimandible showing the strict and intact temporo-mandibular articulation. The photograph was taken after the skull was cleaned and separated from the postcranial elements. The unerupted M_1 and M^1 are held in place despite the fact that their roots were not developed, supporting the interpretation of an undisturbed deposit. The first three cervical vertebrae are rotated but in place, and connected to the foramen magnum.

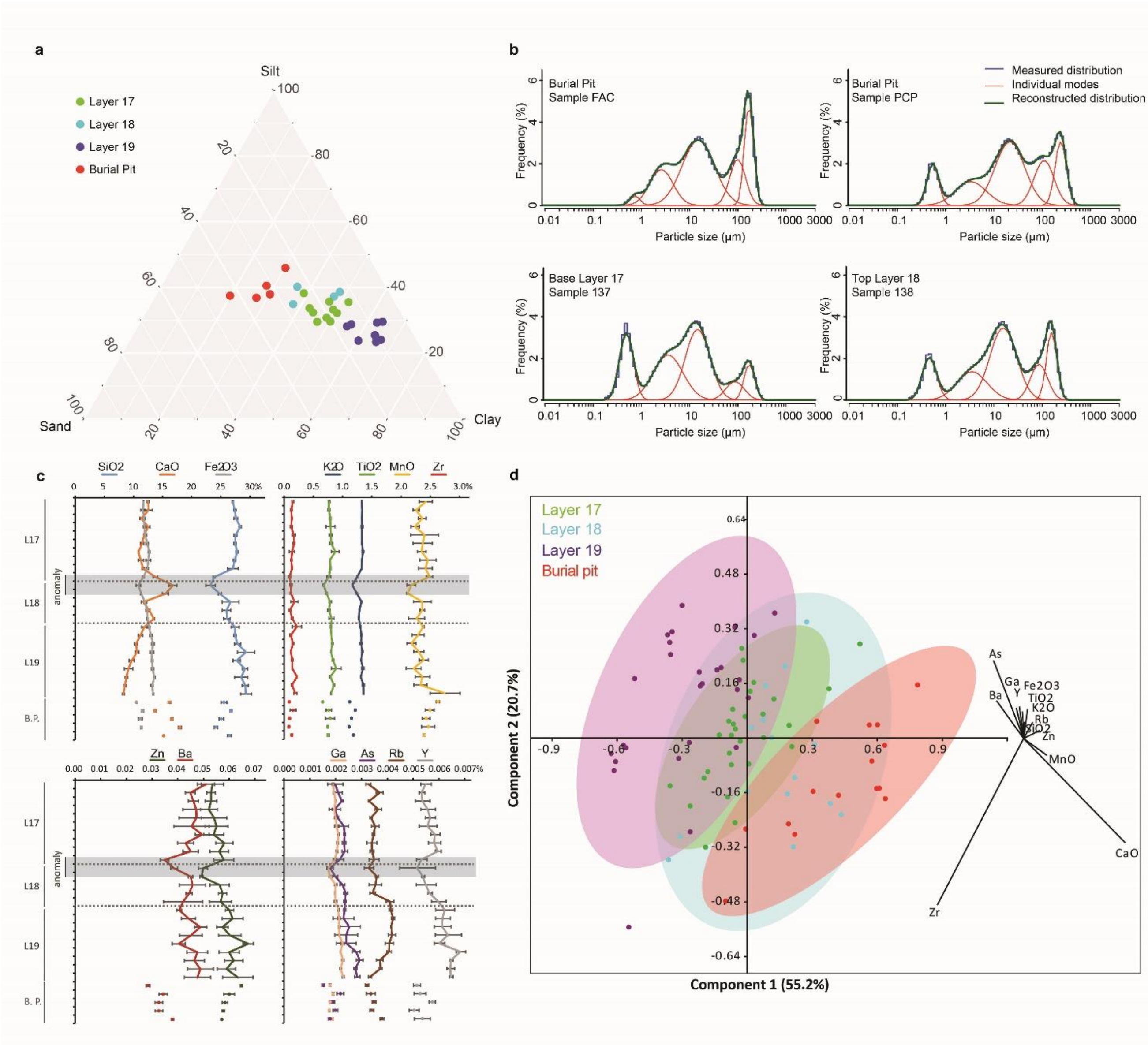

Fig. 3: Analysis of sediment from the stratigraphic sequence and the burial pit. a, Particle size ternary diagram indicating the higher content of sand and silt in the burial pit in comparison to the encasing archaeological layers, and in particular Layer 19. **b**, Examples of particle size distribution and multimodal decomposition showing the similarities of sand and silt modes between the burial samples and samples 137 (base of Layer 17) and 138 (top of Layer 18). **c**, Elemental profiles of sediment from Layers 17, 18, 19 and the burial pit. Element concentrations are expressed in percentages. Sediment samples from the burial pit display an elemental composition remarkably similar to the three samples identified as an anomaly at the top of Layer 18 and the base of Layer 17. **d**, Results of PCA of the centre log ratio data (selected elements: SiO_2, K_2O, TiO_2, MnO, Fe_2O_3, Zn, Ga, As, Rb, Y, Zr and Ba). Confidence ellipses at 95%. The burial pit samples markedly differ from Layer 19.

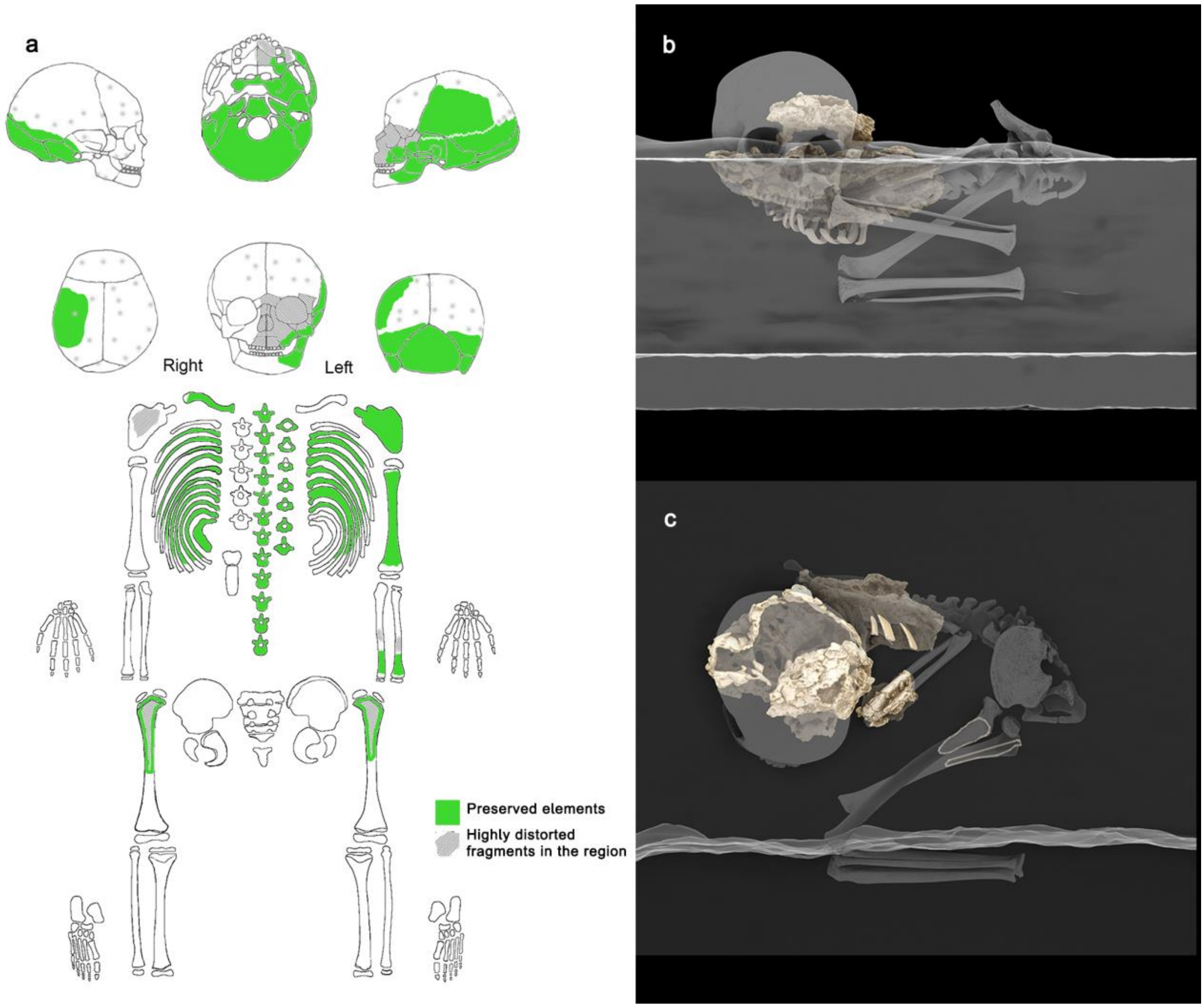

Fig. 4: Mtoto's preservation and position in the pit. a, Preserved parts of the PYS skeleton. Front **b** and top **c** view of the virtual reconstruction of the preserved skeletal parts (solid) superimposed over a transparent comparative skeleton. The fragments of both the left and right femora could not be recovered, but their outline was identified on the plan view and in the wall profile, marked as a solid line over the transparent skeleton. The position of the right radius and ulna fragments and the right parietal are approximate, since they were found detached from the original block.

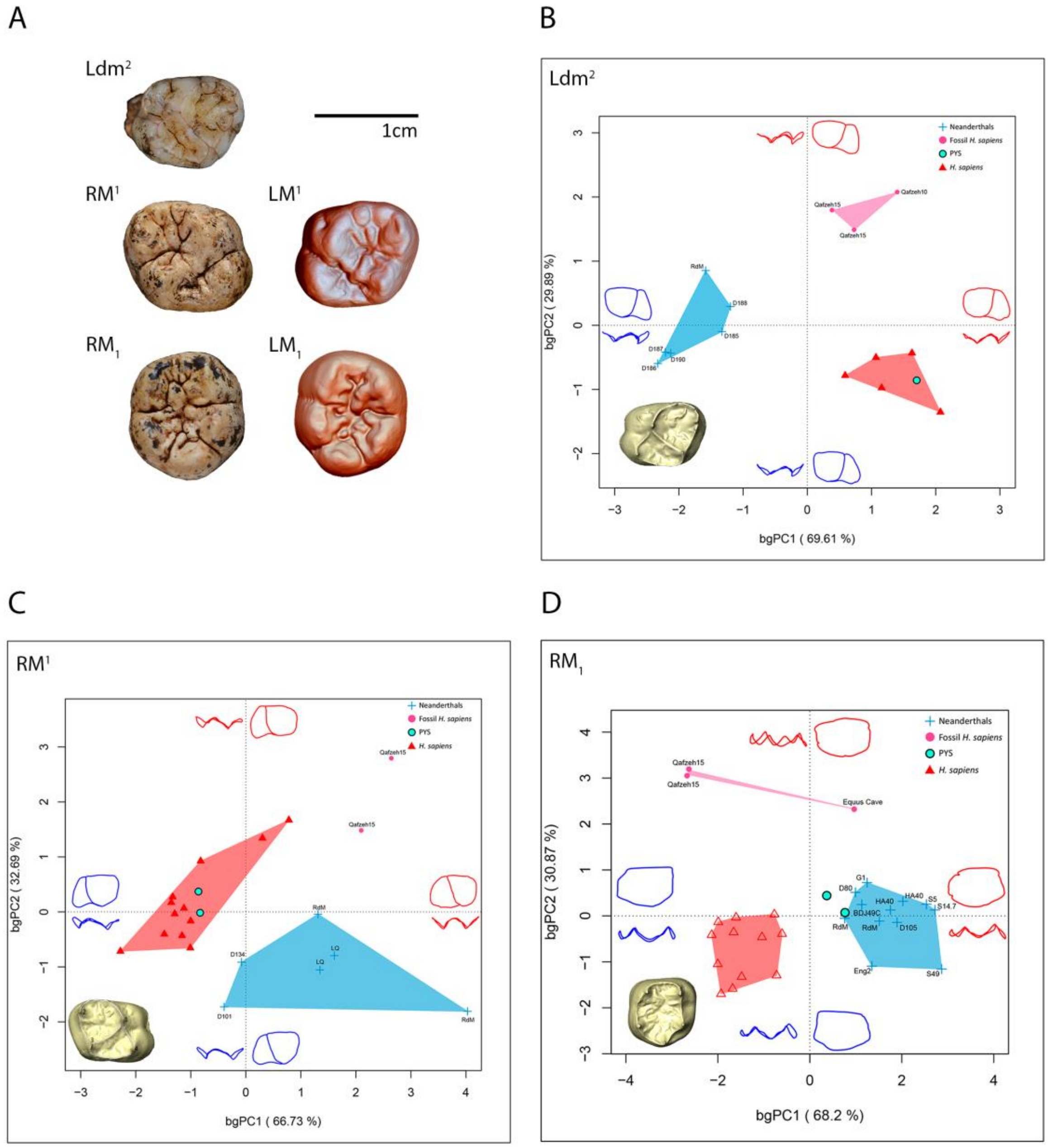

Fig. 5: PYS human dental remains. **a**, PYS dental remains: isolated teeth (left column) and mCT 3D reconstruction of the two molars included in the maxillary and mandibular bones (right column). All molars are positioned with the mesial surface towards the top and the distal surface towards the bottom. L (left); R (right); dm2 (second deciduous molar), M^1 (permanent upper first molar), M_1 (permanent lower first molar). **b**, Between-group principal component analysis (bgPCA) of the Procrustes shape coordinates of the PYS Ldm2 enamel dentine-junction surface (EDJ) compared with to those of Neanderthals (n=6), fossil *H. sapiens* (n=3) and modern humans (n=5). **c**, Between-group principal component analysis (bgPCA) of the Procrustes shape coordinates of the PYS RM1 EDJ compared with to those of Neanderthals (n=6), fossil *H. sapiens* (n=2) and modern humans (n=12). **d**, Between-group principal component analysis (bgPCA) of the Procrustes shape coordinates of the PYS RM1 EDJ compared with to those of Neanderthals (n=12), fossil *H. sapiens* (n=3) and modern humans (n=12).